

Improved Simulations of Biomass Burning Aerosol Optical Properties and Lifetimes in the NASA GEOS Model during the ORACLES-I Campaign

Sampa Das^{1,2} Peter R. Colarco¹, Huisheng Bian^{1,3}, and Santiago Gassó^{2,4}

5 ¹Atmospheric Chemistry and Dynamics Laboratory, NASA Goddard Space Flight Center, Greenbelt, Maryland, USA

²Earth System Science Interdisciplinary Center, University of Maryland, College Park, Maryland, USA

³Goddard Earth Sciences Technology and Research II, University of Maryland, Baltimore County, Maryland, USA

⁴Climate and Radiation Laboratory, NASA Goddard Space Flight Center, Greenbelt, Maryland, USA

Correspondence to: Sampa Das (sampa.das@nasa.gov) and Peter Colarco (peter.r.colarco@nasa.gov)

10 **Abstract.** In order to improve aerosol representation in the NASA Goddard Earth Observing System (GEOS) model, we evaluated simulations of the transport and properties of aerosols from southern African biomass burning sources that were observed during the first deployment of the NASA ORACLES (ObseRvations of Aerosols above CLouds and their intEractionS) field campaign in September 2016. An example case study of September 24 was analyzed in detail, during which aircraft-based in-situ and remote sensing observations showed the presence of a multi-layered smoke plume structure with significant vertical variation in single scattering albedo (SSA). Our baseline GEOS simulations were not able to represent the observed SSA variation, nor the observed organic aerosol-to-black carbon ratio (OA:BC). Analyzing the simulated smoke age suggests that the higher altitude, less absorbing smoke plume was younger (~4 days), while the lower altitude and more absorbing smoke plume was older (~7 days). We hypothesize a chemical or microphysical loss process exists to explain the change in aerosol absorption as the smoke plume ages, 15 and we apply a simple loss rate to the model hydrophilic biomass burning OA to simulate this process. We also utilized the ORACLES airborne observations to better constrain the simulation of aerosol optical properties, adjusting the assumed particle size, hygroscopic growth, and absorption. Our final GEOS model simulation with additional OA loss and updated optics showed better performance in simulating aerosol optical depth (AOD) and SSA compared to independent ground and space-based retrievals for the entire month of September 2016, including the Ozone 20 Monitoring Instrument (OMI) Aerosol Index. In terms of radiative implications of our model adjustments, the final GEOS simulation suggested a decreased atmospheric warming of about 10% (~2 W m⁻²) over the south-east Atlantic region and above the stratocumulus cloud decks compared to the model baseline simulations. These results improve 25 the representation of the smoke age, transport, and optical properties in Earth system models.

1 Introduction

30 Smoke plumes emitted by biomass burning in the southern African region are transported over the southeast (SE) Atlantic during the peak fire season (August-October) every year, and they modify the regional energy budget via direct, indirect, and semi-direct effects of aerosols contained in these plumes (Lu et al., 2018; Gordon et al., 2018; Das et al., 2020). Observation-based estimates of the direct radiative effects (DRE) of aerosol over the SE Atlantic showed that at the top of the atmosphere (TOA) the DRE of biomass burning aerosols for a given set of aerosol optical 35 properties can be positive (that is, radiatively warming) or negative (radiatively cooling), depending on the albedo and coverage of the underlying clouds (Chand et al., 2009; Zhang et al., 2016; Wilcox, 2012; Keil and Haywood, 2003). However, the magnitudes of these observation-based aerosol DRE estimates remain uncertain partly due to the poorly quantified aerosol radiative properties of aerosols above clouds (Kacenelenbogen et al., 2019). For the modeling-based studies as well, there is no consensus on the sign or magnitude of the direct aerosol forcing over this region 40 (Myhre et al., 2013; Schulz et al., 2006). In addition, the aerosol-DRE estimated from satellites typically exceeds model estimates over this region (de Graaf et al., 2020). One of the possible reasons for the DRE mismatch could be that the aerosol optical property assumptions, especially single-scattering albedo (SSA)—which determines aerosol absorption—has large variability among models, and model SSAs were frequently found to be higher than the aircraft measurements (Doherty et al., 2022; Shinozuka et al., 2020; Mallet et al., 2021).

45 Climate models usually derive their aerosol optical properties (extinction coefficient, SSA and phase function) using a database of Mie theory-based calculations (e.g., Optical Properties of Aerosols and Clouds or OPAC (Hess et al., 1998)) available for a range of wavelengths and relative humidity (RH) values, under the assumptions of aerosol mixing state, microphysical properties (size distribution, refractive index, etc.) and water uptake (or hygroscopic

growth factor). In general, these properties (or their functional forms) are prescribed in the model, and especially in models that lack complex aerosol microphysical and chemical representations, these properties represent a hard constraint on the possible parameter space in the model. Furthermore, aerosol properties set in the model near biomass burning sources may not be representative of the changes in aerosol properties during long-range transport of smoke plumes due to changing composition and size, photochemistry, and humidification of aerosol particles (Zhao et al., 2015; Wong et al., 2017; Freney et al., 2010; Cubison et al., 2011).

In this study we investigate the properties of biomass burning aerosols over the SE Atlantic as simulated in the NASA Goddard Earth Observing System (GEOS) model and observed by airborne, space-based, and ground-based measurements taken during the NASA ObseRvations of Aerosols above CLouds and their intEractiOnS (ORACLES) field campaign (Redemann et al., 2021). Recent advances in the GEOS model have improved the representation of aerosol properties, and especially the representation of carbonaceous aerosols (Colarco et al., 2017; see details in section 2.4). We focus in this paper on the results of GEOS simulations made over the period of the ORACLES-I field campaign, which was based out of Walvis Bay, Namibia, during late August-September 2016. The ORACLES-I deployment included two aircraft: the NASA P-3 for full atmospheric profiling and low-to-mid-level in-situ sampling, and the high-altitude NASA ER-2 for remote sensing observations (Figure 1a). The two subsequent phases of ORACLES (August 2017 and October 2018) only had the P-3 aircraft, so the focus on ORACLES-I gives the most data to evaluate our model simulations.

Our specific objective in this study is to use the ORACLES observations to understand and improve the simulated aerosol optical properties in the GEOS model. Significantly, ORACLES-I observations showed variability in the vertical profile of the smoke SSA on several flights, possibly related to smoke plume aging (Dobrucki et al., 2023; Redemann et al., 2021). Here, we utilize the GEOS model to investigate further this issue of SSA variability and present a simplistic approach to capture the observed SSA change within aging smoke plumes for chemistry transport models. After tuning the model aerosol optics and lifetimes based on ORACLES aircraft observations, we utilize the larger spatial coverage of the satellite and ground-based observations to evaluate the model aerosol properties over the complete southern African biomass burning source and outflow regions.

The paper is organized as follows: Section 2 provides a brief description of the observations used in this study along with the description of the model set-up and various capabilities of GEOS that we utilize to complement our analysis. Section 3 discusses the model-data comparisons and the radiative implications of tuning the aerosol properties. Finally, Section 4 summarizes the major findings of our study and discusses future directions for subsequent modeling studies in this regard.

2 Approach and Methods

2.1 ORACLES 2016 Aircraft-based Observations

We provide here brief details of the instruments relevant to our study based on the particle properties measured. Further details of the ORACLES-I instrumentation and related uncertainties are provided in Shinozuka et al. (2020), Redemann et al. (2021), and references therein.

Aerosol Optical Properties: The Hawaii Group for Environmental Aerosol Research (HiGEAR) operated several in-situ instruments on the P-3. These include two Radiance Research particle soot absorption photometers (PSAPs) to measure the aerosol absorption coefficients (at 470, 530, and 660 nm), and two TSI (model 3563) nephelometers (at 450, 550, and 700 nm) to measure the aerosol light scattering coefficients. In addition to the TSI nephelometers, two single wavelength nephelometers (at 540 nm, Radiance Research, M903) were operated concurrently to measure the increase in light scattering as function of RH. The humidified nephelometer was operated close to 80% RH while the dry unit was maintained below 40% (Howell et al., 2006; Pistone et al., 2019). For in-situ SSA or extinction calculation, the measured PSAP absorption was interpolated to nephelometer wavelengths before combining with its scattering data. For both SSA and extinction, we use the corrected or processed data (called SSA_ATP and Exttotal_ATP) that are provided at a time resolution of 1 second within the “merged” files at the ORACLES ESPO Data Archive: <https://espo.nasa.gov/oracles/archive/browse/oracles/id8>, last accessed: 5 December, 2023. Here, PSAP absorption corrections were performed according to an updated algorithm (Virkkula, 2010) and nephelometer measured scattering were corrected according to Anderson and Ogren (1998). The in-situ SSA and extinctions are measured and reported at low (< 40%) RH. Additionally, we only use the measurements for which mid-visible dry extinctions are greater than 10 Mm^{-1} (Pistone et al. 2019).

100 In addition to dry in-situ SSA, we also use the retrievals of column-integrated SSA for ambient conditions from the Spectrometer for Sky-Scanning Sun-Tracking Atmospheric Research (4STAR) instrument, which was also on-board the P-3. 4STAR is an airborne hyperspectral (350-1700 nm) sun photometer which can make direct-beam measurements (sun-tracking mode) for retrievals of partial-column aerosol optical depth (AOD) above flight level (LeBlanc et al., 2020). Under ideal flight and atmospheric conditions, 4STAR can also perform sky scans in either the principal-plane or almucantar (sky scanning mode). The 4STAR sky scans were processed using a modified version of the Version 2 Aerosol Robotic Network (AERONET) retrieval algorithm described in Dubovik and King (2000). However, due to suspected stray light contamination within the 4STAR spectrometer around 440 nm (Pistone et al., 2019), the set of input wavelengths for 4STAR were modified to be 400, 500, 675, 870, and 995 nm (as opposed to the standard AERONET input wavelengths). We used the quality-screened data available at the ORACLES ESPO Data Archive and presented in Pistone et al. (2019), but we further limit our analysis to SSA retrievals that had 110 $AOD_{400\text{nm}} > 0.4$ similar to what AERONET uses in its quality-control criteria. Additionally, we only consider the SSA retrievals for which flight altitude was greater or equal to 1 km, which is about the typical boundary layer height over the ocean for the ORACLES 2016 region. Since 4STAR retrieves the above-aircraft column SSA, our last screening criterion was used to focus on the SSA of smoke layers above the boundary layer and exclude the influence of marine aerosols within the boundary layer.

115 We also use the atmospheric profiling provided by the NASA Langley Research Center High Spectral Resolution Lidar (HSRL-2, Hair et al. (2008)) that was deployed on the ER-2 aircraft. Note that flight paths for the P-3 and ER-2 only partly overlapped (Figure 1a), for example on the September 24 case (Figure 1b) that we analyze in greater detail to utilize this synergy between the two aircraft (Section 3.1). HSRL-2 measures aerosol backscatter and depolarization at 355, 532, and 1064 nm, and aerosol extinction at 355 and 532 nm. Out of the standard aerosol data products (Burton et al., 2012) that HSRL-2 provides, we use the aerosol extinction and lidar ratio (extinction-to-backscatter ratio) profiles at 355 and 532 nm for this study, both provided in 60 second averages to improve the instrument signal-to-noise (equates to ~ 12 km along-track horizontal resolution of the aircraft).

120 **Aerosol Composition:** The Single Particle Soot Photometer (SP2) was deployed on the P-3 as part of HiGEAR to measure the mass of refractory black carbon (rBC) particles by passing a powerful laser beam and heating them to incandescence (Schwarz et al., 2006). The peak value of this incandescence signal has been shown to linearly correlate with the mass of the rBC particle (Stephens et al., 2003). The bulk submicron non-refractory aerosol composition, on the other hand, was provided by the time of flight (ToF) Aerodyne aerosol mass spectrometer (AMS) in the form of organic aerosol (OA), sulfate (SO_4), nitrate (NO_3), and ammonium (NH_4) mass concentrations (DeCarlo et al., 2008). The AMS-measured mass concentrations are provided at standard temperature (273 K) and pressure (1000 hPa), but 130 we convert them here to ambient conditions using the ideal gas law and measured pressure and temperature information before comparing with the model equivalents.

135 **Aerosol Size Distribution:** Particle size distributions used in this study were measured from the P-3 with an ultra-high-sensitivity aerosol spectrometer (UHSAS, Droplet Measurement Technologies, Boulder CO, USA) with a fuselage-mounted inlet. UHSAS is an optical-scattering, laser-based aerosol particle spectrometer that measures particles from 60–1000 nm at 1 s time resolution, thereby covering the entire accumulation mode. The UHSAS measured size distribution is reported as particle number concentrations (in cm^{-3}) per size bins that are approximately logarithmically spaced.

140 **Carbon Monoxide (CO):** CO was measured from the P-3 with a gas-phase CO/CO₂/H₂O analyzer (ABB/Los Gatos Research CO/CO₂/H₂O analyzer known as COMA) with an inlet mounted on the aircraft fuselage. It uses off-axis integrated cavity output spectroscopy (ICOS) technology to make stable cavity enhanced absorption measurements of CO, CO₂, and H₂O in the infrared spectral region (Provencal et al., 2005). The measurements were reported as dry air volume mixing ratios in parts per billion (ppbv).

2.2 Ground-based Observations

145 The Aerosol Robotic Network (AERONET) measures the spectral aerosol optical thickness (AOT) through a ground-based network of sun/sky scanning photometers (Holben et al., 1998). For September 2016, Figure 1a depicts the sites that were operational over southern African biomass burning source regions during ORACLES-I. AERONET provides spectral AOT to an accuracy of ± 0.015 from direct sun measurements. In our analysis we use the Version 3, Level 2 (cloud-screened, quality-assured) AERONET direct sun derived AOT product, specifically the AOT at 500 nm as well as the spectral SSA retrievals at 440, 675, 870, 1020 nm (Giles et al., 2019; Sinyuk et al., 2020).

150 **2.3 Satellite Observations**

2.3.1 OMI Absorbing Aerosol Index

We use space-based aerosol observations from the Ozone Monitoring Instrument (OMI; Levelt et al. (2006)) on board the NASA Aura spacecraft, which flies in a polar orbit with a local equator-crossing time of 13:30. OMI is a hyperspectral (270-500 nm), wide swath (\sim 2600 km) imager that observes the back-scattered solar radiation with a nominal ground pixel size of $13 \times 24 \text{ km}^2$ at nadir and $13 \times 150 \text{ km}^2$ at the swath edges. Aerosol products are from the OMAERUV algorithm (version 1.8.9.1, after Torres et al., (2007)). Fundamental to the OMAERUV retrieval is the so-called aerosol index (AI). The AI is computed from the observed radiances at two channels where ozone absorption is weak (354 and 388 nm for OMAERUV), where the observed spectral contrast is compared to the (easily characterized) spectral contrast expected in a purely molecular atmosphere. Under cloud-free conditions the AI is sensitive to aerosol loading, height, and absorption, where increases in any of those quantities result in a higher positive magnitude value of the AI. The OMI swath ideally provides near-daily global coverage but has been impacted by a “row anomaly” defect since shortly after launch that has effectively degraded its coverage by about 50% so that OMI now achieves global coverage every two days (Torres et al. 2018). In our comparisons that follow we sample model output only where valid OMI data are collected. Owing to its relatively large pixel size OMI data are frequently cloud contaminated. We restrict our analysis to best available data, where the algorithm quality-assurance flag = 0.

2.3.2 MODIS NNR (Neural Net Retrieval)

The Moderate resolution Imaging Spectroradiometer (MODIS) sensors have been flying on two spacecraft, Terra (10:30 local solar time equator crossing) since 2000 and Aqua (13:30 local solar time equator crossing) since 2002. The MODIS collection 6.1 algorithms (namely, dark target land, ocean, and deep blue) retrieve aerosol properties over both ocean and land surface types using the observed spectral reflectance (Levy et al., 2013). However, instead of directly using the MODIS operational retrievals of AOD for model evaluation, we use a bias-corrected AOD dataset, called the MODIS NNR, which was derived initially for use in the Modern-Era Retrospective analysis for Research and Applications, version 2 (MERRA-2, Randles et al., 2017) aerosol reanalysis. As much care as is taken in creating the MODIS standard products, there are nevertheless significant biases related to cloud and land features that must be screened prior to using these data in assimilation systems (e.g., Zhang and Reid, 2006). The NNR refers to a Neural Net Retrieval algorithm that computes AERONET-calibrated AOD from satellite-based radiances, in this case the same MODIS collection 6.1 radiances used in the standard retrieval products. To derive 10-km resolution MODIS NNR AOD, over-ocean predictors include MODIS level-2 multichannel TOA reflectances, glint, solar and sensor angles, cloud fraction (pixels are discarded when cloud fraction $> 70\%$), and albedo derived using GEOS surface wind speeds. Over land, predictors are the same, except a climatological albedo is included for pixels with surface albedo < 0.15 . The NNR algorithm is trained on the log-transformed AERONET AOD interpolated to 550 nm and co-located with MODIS observations of the predictors. Application of the NNR to the MODIS products is found to produce a higher quality AOD product compared to (relatively unbiased) AERONET observations (Randles et al., 2017).

2.4 Model Description

Simulations are performed with a version of the NASA GEOS model (Molod et al. 2015), a global Earth system model used for near-real time weather and aerosol prediction, performing atmospheric analyses, and producing atmospheric and composition reanalyses, among other applications. The configuration of GEOS run in this study includes an atmospheric general circulation model run with the finite-volume dynamical core (FV3, after Putman and Lin, 2007) on a cubed-sphere horizontal grid. The model physics includes the Grell-Freitas deep convection (Freitas et al., 2018; Grell and Freitas, 2014) and Park and Bretherton (2009) shallow convection, the Lock turbulence scheme (Lock et al., 2000), the catchment land surface model (Koster et al., 2000), RRTMG shortwave and longwave radiation (Iacono et al., 2008), and parameterized P-L chemistry (Nielsen et al., 2017). An aerosol-aware single moment cloud microphysics scheme is employed to provide dynamic cloud and ice effective radii (Bacmeister et al., 2006).

The aerosol scheme utilizes an updated version of the Goddard Chemistry, Aerosol, Radiation, and Transport (GOCART) module (Colarco et al., 2010; Chin et al., 2002). GOCART includes the sources, sinks, and chemistry of dust, sea salt, nitrate, sulfate, and carbonaceous aerosols. Dust and sea salt have dynamic (i.e., wind-driven) sources, and for each the aerosol particle size distribution is discretized into a series of five non-interacting size bins. Bulk sulfate mass is tracked, with primary emissions from anthropogenic sources and precursor emissions of dimethylsulfide (DMS), which has a wind-blown source function over the ocean scaled to observed DMS surface

concentrations (Lana et al. 2011), and sulfur dioxide (SO_2), which has emissions from anthropogenic, volcanic, and biomass burning sources. Chemical production of sulfate from precursors uses a simplified OH- $\text{H}_2\text{O}_2\text{-NO}_3$ scheme, with oxidants provided from the MERRA-2 GMI full-chemistry simulation (Strode et al., 2019). Nitrate is represented by three non-interacting size classes and has precursor emissions from anthropogenic, biomass burning, and ocean sources of ammonia. The fine mode nitrate includes heterogeneous formation from nitric acid on dust and sea salt surfaces (Bian et al., 2017). Carbonaceous aerosols are partitioned into three compositional species—black carbon (BC), organic carbon (OC), and “brown” carbon (BR)—where each species is further divided into hydrophobic and hydrophilic modes. In the context of our simulations, “brown” carbon is organic carbon from biomass burning sources, separated from other anthropogenic and biogenic sources of organic aerosol to treat the optical properties distinctly (Colarco et al., 2017). A simplified secondary organic aerosol (SOA) mechanism is employed that scales volatile organic carbon (VOC) emissions in terms of CO emissions from anthropogenic, biofuel, and biomass sources, following Kim et al. (2015), with conversion of VOC to SOA modeled using a simple function of the MERRA-2 GMI-provided OH fields and the SOA going to hydrophilic modes of organic and brown carbon. Biogenic sources of SOA are from an online version of the MEGAN (Model of Emissions of Gases and Aerosols from Nature) mechanism running inside GEOS. Baseline optical properties are primarily based on the OPAC (Hess et al. 1998) database (see also Chin et al., 2002) with the optical properties for non-spherical dust particles based on Colarco et al. (2014) and the optical properties of brown carbon based on Colarco et al. (2017). Optical properties are defined in pre-computed lookup tables that are a function of species, wavelength, and relative humidity (to account for particle humidification).

In-situ optical quantities such as extinction and SSA are computed by summing across the aerosol species concentrations as scaled by the appropriate optical property (e.g., mass extinction efficiency). Column integrated optical quantities (e.g., AOD and SSA) are computed as the vertical integral of the in-situ properties. The aerosol species are externally mixed in the model for optics and chemistry purposes.

Biomass burning emissions in our simulations are based on the Quick Fire Emission Dataset (QFED; Darmenov and da Silva, 2015). QFED utilizes satellite fire radiative power observations from MODIS Level 2 fire products and scales them using biome-specific emission factors to aerosol and trace gas emission fluxes. In this study we particularly use QFED emission products for SO_2 , CO, NH_3 , BC, and OA. Here and throughout the rest of the paper, model OA refers to organic aerosol contributions from all sources (biomass, biogenic, biofuel and anthropogenic) unless specifically mentioned.

Our baseline GEOS simulation is performed at a c360 (~25 km) horizontal resolution with 72 vertical hybrid sigma levels extending from the surface to ~80 km altitude. The model is “replayed” to the European Centre for Medium-Range Weather Forecasts (ECMWF) fifth generation atmospheric reanalysis (ERA5, Hersbach et al., 2020). “Replay” mode is like running the model in an atmospheric data assimilation mode, but instead of ingesting the meteorological observations directly we use the atmospheric state (surface pressure and vertical temperature, humidity, and horizontal wind components) from a prior analysis and compute the model incremental analysis update (IAU) from the forecast model background state versus that analysis, in this case versus ERA5. This approach allows us to perform a simulation constrained by realistic meteorology at a fraction of the cost of performing the full atmospheric data assimilation cycle. ERA5 was chosen to replay against versus the GEOS-native MERRA-2 (Gelaro et al., 2017) because sensitivity simulations (not presented here) showed a more favorable representation of the smoke plume vertical distribution transported from southern Africa (see also Das et al. (2017) for a discussion of the challenges of models in representing the vertical profile of smoke in this region). Table 1 summarizes the suite of GEOS simulations performed in this study, described in subsequent sections of the text.

Table 1. Summary of GEOS simulations performed in this study.

Simulation Name	Description
Baseline	Default version of the GEOS model
Smoke Age	Default version of the GEOS model run with biomass burning OA tagged by day of the week emitted (Section 2.4.1)
Smoke Composition	Default version of the GEOS model run with biomass burning OA tagged by type of vegetation burned (Section 2.4.2)
OA-loss	Hydrophilic OA from biomass burning is assigned a 6-day e-folding loss time; OA from biomass burning sources is enhanced 60%, BC from biomass burning sources is enhanced 15%
OA-loss+updated optics	As in OA-loss but with updated aerosol optical properties

245 **2.4.1 Estimation of Physical Smoke Age**

Our “Smoke Age” simulation (see Table 1) has the brown carbon tracer “tagged” in such a way as to determine the day of the week on which its emissions were injected. Effectively, eight instances of the biomass burning organic aerosol are tracked in this simulation (seven instances, one for emissions occurring each day of the week, and an eighth for the cumulative total emissions). The “Monday” tracer, for example, resets the tracer concentration globally to zero when the model clock ticks over to Monday at 0 UTC. The differences between the total and individual day-of-the-week tracers allows determination of the smoke age out to smoke emitted seven days previously. The simulation is otherwise identical to our baseline simulation.

250 **2.4.2 Estimating the Smoke Composition based on their Emission Source Vegetation Type**

Our “Smoke Composition” simulation has the biomass burning OA tagged by the vegetation source burned based on the QFED inputs. QFED biomass burning emission sources are classified using the land cover or vegetation type information provided by the MODIS Land Cover Type Product (MCD12C1, IGBP classification scheme, Friedl et al., (2010)) for the year 2016, shown in Figure 2. The MCD12C1 product supplies global maps of land cover at annual time steps at 0.05° spatial resolution in geographic latitude/longitude projection. Further details on the Collection 6 MODIS Land Cover products, including MCD12C1 are provided in their User Guide: https://lpdaac.usgs.gov/documents/101/MCD12_User_Guide_V6.pdf, last accessed: 5 December, 2023. We define six major vegetation or land cover (LC) types over central and southern Africa that could contribute to the smoke over ORACLES region: (1) savannas (LC type 9), (2) woody savannas (LC type 8), (3) grassland (LC type 10), (4) tropical forest (LC type 2, 4, 5), (5) shrubland (LC type 6,7) and (6) croplands (LC type 12, 14) (Figure 2). We then define seven instances of brown carbon tracers (six are “tagged” based on their emission source vegetation type, plus one for the total) within the model to be able to investigate the contributions of each of these vegetation types towards the smoke observed over the ORACLES region.

260 **2.4.3 OMI AI Simulator**

We employ a radiative transfer code to simulate the OMI aerosol index (Buchard et al., 2015; Colarco et al., 2017). Similar to the computation of the model AOD, the AI simulator takes as input the GEOS-simulated aerosol mass distributions and meteorological fields, and—subjected to the GEOS aerosol optical property assumptions—simulated OMI radiances are calculated at the OMI viewing conditions (viewing geometry, terrain height, and surface reflectance). AI is then calculated as in Colarco et al. (2017). Because we do not explicitly simulate the impact of modeled cloud fields on the simulated radiance, we restrict our comparisons to the highest quality OMI retrievals (formally, QA-flag = 0) to eliminate as much as possible cloud pixels in the satellite product impacting our comparisons.

270 **2.5 NOAA HYSPLIT Model with ERA-5 Meteorological Fields**

We use the Linux-based distribution of the NOAA (National Oceanic and Atmospheric Administration) Hybrid Single-Particle Lagrangian Integrated Trajectory (HYSPLIT, v5.2.1) model (Rolph et al., 2017; Stein et al., 2015) to understand the transport pathway and origin source locations of the smoke observed during ORACLES 2016. ERA-5 meteorological data is used to drive HYSPLIT so that the trajectories calculated are consistent with our GEOS simulations. We employ the meteorological grid ensemble approach within HYSPLIT to quantify the uncertainty and divergence associated with the trajectory calculations. In this method, trajectories are computed for a 3-dimensional cube centered on the starting point. Instead of moving the trajectory initial location about the starting point, however, all the trajectories start from the initial point but the driving meteorological data for each trajectory is offset slightly from that central location (see https://www.ready.noaa.gov/documents/Tutorial/html/traj_ensem.html, last accessed: 7 December, 2023). Default offsets are chosen, so that the meteorology is spread one grid box in the horizontal (~25 km) and about 250 m in the vertical. This results in 27 members of the trajectory ensemble for all possible offsets in X, Y, and Z directions in space.

280 **3 Results and Discussions**

In the following we analyze the ORACLES airborne data and our GEOS simulations, first for the specific case of the aerosol plume flown by the P-3 and ER-2 on September 24, 2016. Refinements to our simulations are then described. We conclude by summarizing our simulation of the entire month of September 2016 in the context of

ground-based and space-based remote sensing observations and estimate the total aerosol radiative forcing during the month.

295 **3.1 24 September 2016 Case**

We focus here on the September 24, 2016, smoke plume observed from both the P-3 and ER-2 aircraft (Figure 1b). We choose this day for two main reasons: (1) the presence of multi-layered smoke around 12°S and 11°E that showed a gradual but substantial change in in-situ measured SSA vertically (from 0.83-0.91 over 1-5.5 km respectively) that GEOS was unable to capture in our baseline simulation, and (2) to utilize the synergy of multiple instruments onboard both the P-3 and ER-2 aircraft as they sampled the same locations for a significant part of their flight.

On September 24 the P-3 flew an out-and-back south-to-north-to-south flight along 11°E longitude to and from Walvis Bay, Namibia (Figure 1b). The P-3 vertical flight profile is shown in Figure 3 with the in-situ (PSAP and nephelometer) measured dry extinction superimposed on the baseline GEOS-simulated extinction profile sampled in space and time along the flight track. The out-and-back nature of the flight track is evident in the model fields, which show a quasi-symmetric vertical profile in time. The blue stars on Figure 3 indicate the location of 4STAR sky-scans for which quality screened column-integrated SSA were retrieved (Pistone et al., 2019). On the same day the ER-2 aircraft carrying the HSRL-2 lidar spatially overlapped geographically with part of the P-3 flight path (Figure 1b). The retrieved and GEOS-simulated vertical aerosol extinction profile (GEOS sampled along the ER-2 track) are shown in Figure 4. A similar aerosol plume structure is apparent in GEOS comparisons to these two sets of observations (Figures 3 and 4).

Between 1245 and 1301 UTC the P-3 sampled a multi-layered smoke plume around 12.3°S and 11°E while descending from 6 km to 1 km. The ER-2 flew over the same location earlier in the day, and this common spatial region is shown by the black rectangular box in Figures 3 and 4 and is indicated by the green star in Figure 1b. For purposes of comparison, we averaged the ER-2 HSRL profiles over the same area covered during the P-3 profile (from 915 to 930 UTC, black box in Figure 4). We compared the observed aerosol extinctions for this profile based on in-situ instruments (Figure 5a) and HSRL-2 lidar (Figure 5b) with our GEOS baseline simulation. The in-situ observations are made under dry conditions (RH <= 40%), while the lidar observations are at ambient conditions. An elevated smoke layer was observed from both aircraft between 4 – 6 km altitude and a lower layer between about 1.5 – 3.5 km altitude. Figure 5c shows the P-3 measured temperature for this profile, as well as the dry and moist adiabats anchored at 2 km. The slope of the observed temperature profile is greater than the dry adiabatic lapse rate but less than the moist adiabatic lapse rate, indicating conditionally stable air layers that explain the distinct plumes over the ocean, also a feature over land (Tyson et al. 1996). Additionally, the high relative humidity at the upper layer (RH ~ 80%, Figure 5c) suggests humidification could be part of the explanation for the higher aerosol extinction (peak extinction ~ 100 Mm⁻¹ at 4.5 km altitude) compared to the in-situ measurement (~ 150 Mm⁻¹ at the same altitude). The GEOS simulated dry extinction is underestimated compared to the in-situ data (peak of ~ 100 Mm⁻¹) but has a better match with HSRL-2 retrieval at ambient conditions (~ 175 Mm⁻¹), at least for the upper-level smoke layer. The model profile of humidity agrees well with the observations (Figure 5c), so the difference in extinction suggests that the model has more hygroscopic growth of the smoke for the higher altitude plume than the observations suggest, a point we will return to later. The model-simulated ambient extinction is underestimated for the lower aerosol layer despite a good match of simulated RH with the observations overall (Figure 5c).

We compare the observed and simulated SSA on this profile in Figure 5d. The in-situ measurements of dry SSA at 550 nm showed a gradual decrease in values from about 0.92 to 0.84 between the altitudes of 5.5 km to 1 km respectively. The model simulations of SSA, on the other hand, showed some decrease from the aerosol layer centered around 4.5 km to the lower altitude layers but stayed fixed at about 0.89 from 4 km to 1 km altitude. Clearly the baseline GEOS model does not simulate the observed vertical variability in SSA.

335 **3.1.1 Composition, SSA and Relation with Simulated Smoke Age**

To understand the vertical variations in SSA, we first analyze the smoke composition of this September 24 profile by comparing the model-simulated aerosol mass concentrations to the corresponding measurements from the AMS and SP2 in-situ instruments (Figure 6). Organic aerosols (from all sources) contribute about 65-70% of the total aerosol mass, followed by nitrates, sulfate and BC, respectively in both model and the observations. Model-simulated aerosol composition agrees well with in-situ observations, especially for the top plume centered around 4.5 km (where both show peak OA mass concentration ~ 17 $\mu\text{g m}^{-3}$). OA is overestimated by the model for altitudes below 2.5 km (Figure 6a), while nitrates are underestimated for the same altitudes (Figure 6c). Sulfate (Figure 6d) and BC (Figure

345 6b) show a similar profile to the simulated OA but are present at lower concentrations than the observations suggest, particularly for the lower altitude layer. Sulfate is about half the concentration in the model as observed. BC has similar concentration to the observations for the higher smoke plume ($\sim 1 \mu\text{g m}^{-3}$) but is only about half the concentration of the observations in the lower layer. Except for nitrate, the observed multi-layer structure for this profile is evident in the model species.

350 SSA strongly depends on the relative amounts of scattering to absorbing aerosols. BC is the primary absorbing component at 550 nm in the smoke plumes simulated here, while OA, nitrates and sulfates are mostly scattering. Given that the SSA is changing with altitude (Figure 5d) and multiple plumes are observed within the vertical profile (Figure 5a), we investigate two things: (1) the smoke age in the vertical, and (2) how the relative aerosol composition varies with altitude and smoke age. Figure 7a shows the model-simulated, extinction-weighted mean smoke age for our 355 September 24 profile using our “Smoke Age” tagged tracer run (described in Table 1 and Section 2.4.1). Figure 7a also shows the smoke age derived using the WRF-AAM (Weather Research and Aerosol Aware Microphysics) model (Saide et al., 2016) that was used for forecasting and flight planning during the ORACLES campaign (Redemann et al., 2021). Both GEOS and WRF-AAM models have a similar overall structure of simulated plume age, showing minimal smoke age around the center altitude of the upper smoke plume (~ 4 days at 4.5 – 5 km altitude) and higher 360 smoke age at lower altitudes, with a local maximum of about 5 – 6 days between 3 – 4 km and increasing to 7 – 8 days below 2 km. We also show the smoke age distribution from our GEOS “Smoke Age” run at three different altitudes of the profile to clarify the interpretation of the mean smoke age number and to note some of the limitations 365 of model-calculated smoke age (Figure 7b). For example, for the youngest smoke plume centered at 4.5 km, even though the mean smoke age is calculated as 4.1 days, about 40% of the smoke is 1-2 days old and about 20% of the smoke is older than 7 days, suggesting quite a wide distribution. At 3 km altitude the lower mode of the smoke age 370 distribution peaks at 2-3 days old, and at 2 km at 3-5 days old. We should also be mindful that different age distributions could lead to a same mean age value. Finally, for GEOS, we are restricted by the way we track the smoke age that we can only resolve smoke age up to 7 days, and older smoke is lumped into this last bin of our histogram so that the effective age computed is slightly younger than if we could account for all possible smoke ages. Nevertheless, the simulation shows the presence of generally younger smoke at the higher altitudes and older smoke at the lower altitudes.

375 Next, we investigate how the relative composition of aerosols changes with smoke age, and if we can further use that relation to explain the vertical variations of SSA as well. Figure 8a shows the simulated and observed change in SSA with the GEOS-simulated mean smoke age for the profile shown in Figure 5d, and this variation is almost identical to the SSA variation in the vertical since smoke age and altitude are strongly but negatively correlated. The initial drop in SSA between 4 - 5.5 days estimated smoke age is correlated with a simultaneous decrease in OA and nitrates with respect to BC (Figures 8b&c). After 5.5 days age the nitrates are essentially constant in time, and so further decrease in SSA with smoke age is more clearly correlated with a continued decrease in OA:BC ratio (Figure 380 8b). The model captures the variation in $\text{NO}_3:\text{BC}$ and $\text{SO}_4:\text{BC}$ ratio well for most parts of the profile (Figures 8c&d). The major discrepancy between the model and observations lies in the inability of the model to simulate the observed OA:BC variation, which changes in the observations from about 15 (for 4-day old smoke) to about 5 (for 7-day old smoke), whereas the model is essentially constant at a OA:BC ratio of 15. Figures 8e&f show, respectively, the correlation of OA:BC with SSA ($r = 0.89$) and $\text{NO}_3:\text{BC}$ with SSA ($r = 0.88$).

385 The model’s failure to simulate the observed OA:BC ratio variability with age is correlated with its failure to simulate the observed variability in SSA. In the following we consider two hypotheses to explain the age-related variation in the OA:BC ratio. In the first we consider the possibility that smoke of different ages may be originating from different source regions with different emissions of OA and BC. In the second we consider the possibility that there is some unsimulated mechanism for the loss of OA during transport that is related to its age.

3.1.2 Are Smoke Layers Originating from Different Emissions Sources or Burning Conditions?

390 The first hypothesis we examine is whether smoke of different ages is originating from different source regions with different characteristics in the composition of emitted species or different proportions of flaming to smoldering phase of the combustion products. We use three approaches to examine this hypothesis: (1) we generate ensembles of back-trajectories to track the origin of smoke layers at different vertical levels, (2) we utilize the vegetation type “Smoke Composition” tracer run of our GEOS model (Table 1, Section 2.4.2) to quantify the contribution of each 395 vegetation type towards OA amounts (or extinction), and (3) we examine the observed black carbon to carbon monoxide ratios as an indicator of whether the smoke arises from flaming versus smoldering combustion. Our analysis is for the same September 24 aerosol profile discussed previously.

GEOS uses biomass burning emissions from the QFED inventory, based on the MODIS fire radiative power products (Section 2.4). QFED provides daily, gridded biomass burning emission fluxes of relevant species, such as OA, BC, and SO₂. Figure 9a shows the QFED emission locations and cumulative amounts of OA emitted over the seven days prior to September 24. Figures 9b&c show the HYSPLIT-model generated ensemble back trajectories (multi-colored lines) initialized from two different vertical levels (4.5 km versus 2 km) that represent the location of the two distinct smoke plumes evident in the profile plots (e.g., Figure 6a). For the higher-altitude smoke layer (centered around 4.5 km), the clustering of the trajectories and their intersections with the surface (where they would entrain smoke) occurs only a few days before intercepting our profile location (the black star in Figure 9b, at 12°S, 11°E), consistent with the smoke being young (about 4 days old, Figure 7). By contrast, the lower-altitude initialized back trajectories (originating at 2 km, Figure 9c) intercept the surface several days back and further to the east of the profile location, consistent with the smoke at these levels being older (about 6-7 days old, Figure 7).

The trajectory information alone does not tell us that the composition of the smoke in the two different layers is similar. Our “Smoke Composition” simulation (see Table 1 in Section 2.4) is used to distinguish the contributions of individual vegetation types to the total smoke composition. QFED distinguishes among several different vegetation types according to land use datasets, and vegetation-dependent emission factors are used to scale from biomass burned to emissions of specific species (i.e., OA and BC). In the “Smoke Composition” simulation we “tag” the smoke emissions from each vegetation type so we can track its evolution separately. In Figure 10a we quantify the contributions of emissions from individual vegetation types to the smoke composition at our profile location, separately for altitudes of 4.5 and 2 km, the central altitudes of the two smoke plumes in the profile. Our results indicate that the major emission sources for both smoke layers are savannas, woody-savannas, and grasslands. The contributions from other vegetation types (tropical forests, shrublands and croplands) amount to only about 20% of the total emissions. More importantly, the contributions from all vegetation types, except grasslands and woody-savannas, are comparable for both the higher and lower-level smoke plumes. The higher grassland contributions (relative to woody-savannas) for the 2 km level are possibly due to smoke originating from the grassland-dominated regions south of 15°S and east of 20°E based on the 2 km back trajectories (Figure 9c) and the land cover map (Figure 2). However, both Akagi et al. (2011) and Andreae, (2019), which are the key databases that most global models use for their assumptions of emission factors of different biomass burning species, do not differentiate between grasslands and savannas as fuel types, assigning them both the same emission factors. After savannas and grasslands the next most prevalent vegetation type contributing emissions is forest, which has a higher OA:BC emission ratio than grasslands and savannas, but contributes only about 10% to the total smoke load and is similar in contribution for both plumes. Crop and agricultural residue have distinct OA:BC ratios (that are highly uncertain, see Table 2) but are an even smaller contribution to the total aerosol load and are also a similar contribution to each layer.

Table 2. Emission ratios for different fuel types relevant to southern African biomass burning region based on two primary databases that most global models use. Akagi et al. (2011) and Andreae (2019) report emission factors for OC and BC, from which we compute the OC:BC ratio. Also shown is the OA:BC ratio used in the GEOS simulations. GEOS assumes OA:OC ratio of 1.8, based on airborne mass spectrometry measurements (Hodzic et al. 2020).

Biomass Burning Fuel Types	Mean OC:BC Emission ratio	OA:BC (= 1.8*OC:BC)	References
Savanna and Grasslands	7.08	12.74	Akagi et al. (2011)
	5.67	10.2	Andreae (2019)
Tropical Forest	9.06	16.3	Akagi et al. (2011)
	8.63	15.5	Andreae (2019)
Agricultural or Crop residue	3.07	5.52	Akagi et al. (2011)
	11.70	21.0	Andreae (2019)

Finally, differences in OA:BC ratio could also be due to different combustion characteristics of the source fires (i.e., flaming versus smoldering), wherein flaming fires are known to generate a lower concentration of organic carbon particles but a higher concentration of BC than smoldering fires (Christian et al., 2003; Yokelson et al., 2009). We

note here that we currently do not make the distinction in emission ratios based on fire characteristics within QFED or GEOS. Vakkari et al. (2018) suggests that excess BC to excess carbon monoxide ratio ($\Delta BC/\Delta CO$ or BC:CO here onwards) can be used as a reliable marker to assess the combustion characteristics, especially for diluted and aged plumes. An increasing $\Delta BC/\Delta CO$ value is indicative of increasing flaming fraction during the burning (Yokelson et al., 2009). Precisely, Vakkari et al. (2018) distributed the BC:CO ratios into bins of 0.005 to represent fires of similar characteristics. Further, based on their measurements over southern African savanna and grassland regions, they found that $BC:CO < 0.005$ represents predominantly smoldering conditions, while $BC:CO > 0.010$ represents predominantly flaming conditions. We consider background CO as 100 ppbv based on the values outside the plume (found at altitudes > 6 km, see Figure 10b) for the September 24 case. Figure 10c shows that the excess BC:CO ratio has very little variation in the vertical and the values are within the range of 0.005-0.010, thereby suggesting approximately an equal mix of smoldering and flaming combustion conditions at altitudes between 1 and 5.5 km.

Based on the analyses shown here we conclude it is unlikely that the observed differences in smoke composition (that is, the OA:BC ratio, as in Figure 8b) at different vertical levels are due to differences in either the burning source vegetation type or combustion conditions.

3.1.3 Implementation of Additional OA Loss Rate

The second hypothesis we consider is that there is a chemical or microphysical loss of OA during transport that is related in some way to the smoke age. OA from biomass burning sources is composed of primary organic aerosol (POA) directly emitted from the burning biomass and SOA formed via oxidative processing of organic gases. As the biomass burning plume ages in the atmosphere, the oxygenation of OA (reflected in O/C ratio) is reported to increase significantly in almost all studies, suggesting strong chemical transformation of OA with aging and formation of more oxidized OA that are compositionally different than POA (Capes et al., 2008; Jolley et al., 2012; Cubison et al., 2011; Forrister et al., 2015; Zhou et al., 2017). OA mass is increased by SOA formation but can also be balanced out by dilution and subsequent evaporation to the gas phase of semivolatile components, resulting in loss of POA mass (Cubison et al., 2011; May et al., 2015; Zhou et al., 2017). In addition, the volatilities of organic species are affected by atmospheric oxidation reactions. In the gas phase, two main processes can affect the volatilities of organics during atmospheric oxidation: fragmentation and functionalization. Fragmentation refers to the loss of carbon from the organic particles, whereas functionalization refers to an increase in particulate oxygen due to the addition of polar functional groups. Therefore, fragmentation leads to an increase in vapor pressure (i.e., the organic compounds become more volatile), while functionalization leads to lowering of vapor pressure of the organic compounds. In the condensed phase, additional bimolecular processes, such as accretion/oligomerization reactions can also affect volatility (Kroll et al., 2009). Changes of OA composition with aging inevitably lead to changes to OA optical and hygroscopic properties and thus have climate implications. The reasons for the variability across studies may be related to variations in fuels burned and combustion conditions, variation in key co-emitted species such as NO_x, and differences in environmental conditions such as dilution rate and temperature and humidity (Shrivastava et al., 2017).

Within GEOS, the OA:BC ratio is prescribed at the point of emission based on the fuel type and related emission factors (see discussion in Section 3.1.2). Further, OA is emitted as 50% hydrophobic and hydrophilic, respectively, while BC is emitted as 80% hydrophobic and 20% hydrophilic. Once emitted, both OA and BC undergo hydrophobic-to-hydrophilic conversion with a conversion rate or e-folding time of 1-2 days (Colarco et al., 2010). This hydrophobic-to-hydrophilic conversion can change the OA:BC ratio somewhat from what it is at emissions due to wet scavenging, but for older smoke (> 2 days old), we do not account for any additional OA or SOA loss due to any microphysical or chemical processes. Indeed, our simulated OA:BC ratio remains mostly constant over time, as in Figure 8b.

With the present model limitations in mind, we introduce an ad hoc loss process for the hydrophilic OA in our model. We additionally increase our overall emissions of biomass burning produced OA to compensate for this added loss channel to approximately preserve the overall regional extinction and AOD. Sensitivity studies suggest a six-day e-folding time applied to the biomass burning hydrophilic OA, with a corresponding increase of about 60% in emissions of OA and about 15% in the BC emissions from biomass burning greatly improves our simulated OA profile (Figure 11a). When these factors are applied to our simulations (“OA-loss” simulation, Table 1), we can simulate well the observed SSA variation with altitude (Figure 11b). Simultaneously, these changes resulted in overall more absorbing aerosol mixtures. Overall, there is better agreement in the SSA between 4STAR and the OA-loss simulation than 4STAR and the Baseline, except at the shortest wavelength (Figure 11c, where at 400 nm we have $SSA_{4STAR} = 0.88$, $SSA_{Baseline} = 0.87$, $SSA_{OA-loss} = 0.86$ and at longer wavelengths the $SSA_{OA-loss}$ is closer to 4STAR than the Baseline by a magnitude of 0.02; see also Table 3).

Table 3. Comparison of the observed and modeled mean SSA between 4STAR and GEOS experiments at 400, 500, and 675 nm.

Wavelength (nm)	Mean SSA			
	4STAR observations	GEOS baseline	GEOS OA-loss	GEOS OA-loss+updated optics
400	0.88	0.87	0.86	0.87
500	0.86	0.90	0.88	0.88
675	0.84	0.89	0.87	0.85

3.2 Updated Optics: Adjusting OA Size Distribution, Hygroscopicity, and Absorption

The previous section focused on the simulation of the aerosol lifecycle and mass distributions with emphasis on the profile flown on September 24, 2016. Here we broaden our use of the ORACLES dataset to better constrain the simulation of optical properties. As briefly described in Section 2.4, the model-derived aerosol optical properties (e.g., extinction coefficients, SSA and phase function) for each aerosol component depends on the assumptions of their microphysical (size distribution, refractive index, etc.) and hygroscopic (or water uptake) properties. Therefore, we use the ORACLES dataset to first evaluate and then adjust three key model assumptions in this regard to improve the model agreement with the observations. Since OA contributes to about 60-70% of the smoke plume mass observed during ORACLES (Figure 6), only the particle properties of biomass burning OA/brown carbon component in the model were adjusted.

The first adjustment was made with respect to the particle size distribution. Within GOCART, a single-mode lognormal size distribution for the OA component is assumed, defined by a number mode radius (r_n) and geometric standard deviation (σ). The baseline model assumption for OA number size distribution (Figure 12, red dashed line) shows a $r_n = 0.021 \mu\text{m}$ and $\sigma = 2.2$ based on Chin et al. (2002). The comparison with UHSAS-measured particle size distribution for the available flight days shows that the observed particle size distribution (for accumulation mode) has a larger mode radius and narrower distribution than the model baseline assumption and does not show much variation amongst different flight days. Nonetheless, we limit the observations to the altitudes between 1-5 km and OA concentration greater than 4 mg m^{-3} to ensure the presence of smoke particles. Therefore, for the updated optics case, we fit a lognormal distribution to the UHSAS-measured size distributions with a $r_n = 0.09 \mu\text{m}$ and $\sigma = 1.5$ (Figure 12).

The second change is related to the model assumption of particle hygroscopicity. We utilized the dry and humidified nephelometer-measured scattering coefficients during ORACLES-I to obtain the scattering enhancement factor, $f(RH)$. The $f(RH)$ is defined as the particle light scattering coefficient at elevated RH divided by its dry value. We consider 80% and 10% as the high and low RH, respectively, and hence consider only those measurements that were obtained closest to these RH values before comparing with the model-derived $f(RH)$ values at the same flight location (Figure 13a). Additionally, to ensure the presence of smoke plumes, we only consider measurements that were made between 1.5-6 km altitude levels. Figure 13a showed that GEOS baseline case significantly overestimates the observed $f(RH)$ by almost a factor of 2. This model overestimation in $f(RH)$ has also been previously reported in multi-model evaluation studies of Doherty et al. (2022) using the ORACLES dataset itself, and in Burgos et al. (2020) using a global dataset of surface-based in situ measurements. Note that the modeled $f(RH)$ presented here has contributions from a combination of smoke aerosol species. For GOCART, except for dust, all aerosol components are considered to have different degrees of hygroscopic growth rate with ambient moisture. We show the hygroscopic growth assumption for three major smoke aerosol components (organics, black carbon, and sulfate) in Figure 13b based on the default optics table used within GOCART. Sulfate hygroscopic growth factor increases most rapidly with increasing RH, followed by organics and least rapidly for black carbon. Therefore, for the “OA-loss” model case (Section 3.1.3), where relative contribution of BC is enhanced for the aged plumes compared to OA, we see a slight reduction in modeled $f(RH)$ compared to observations (Figure 13a). An additional, but minor reduction in modeled $f(RH)$ is observed when the above-mentioned particle size distribution adjustments are made for the organic aerosol component in the model. Finally, we consider that the hygroscopic growth of OA is the same as for BC, and here we see the closest match to observations (a reduction of the simulated $f(RH)$ from greater than 2 to about 1.7, compared to the value of 1.4 determined from the observations, see Figure 13a and also the reduced ratio of the simulated-to-observed $f(RH)$), and so this comprises our second adjustment to model assumption of OA properties.

535 The third and final adjustment to the model optical properties is related to aerosol absorption, which is mainly
characterized by the imaginary part of the complex refractive index (k) of the aerosol component. This change was
motivated by our finding that our model-derived lidar ratios (that is, the ratio of extinction to backscatter) of the smoke
plumes were much higher than the observed values based on HSRL-2 measurements from the ER-2, especially in the
355 nm channel (70 sr versus 85 sr) for the model baseline case (Figure 14a). A previous study by Veselovskii et al.
540 (2020) that used the Raman Lidar observations over Senegal in West Africa for their analysis, also found that the
GEOS modeled lidar ratios were consistently higher compared to their lidar observations for a range of relative
humidity, when the model k in the UV was set to its baseline value (of $k_{350} \sim 0.05$). The aerosol backscattering
coefficient is more sensitive to the absorption than the extinction coefficient because an increase in absorption is
545 accompanied by a decrease in scattering. Thus, we expect that decreased absorption of OA in the UV should lead to a
decrease in the lidar ratio. Figure 14 demonstrates the sensitivity of the lidar ratios to the changes in the imaginary
component of the refractive index. The baseline optics table assumes $k_{350} = \sim 0.05$, and so clearly reducing k_{350} to 0.01
550 or 0.02 provides a better match of the model lidar ratio with the HSRL-2 observations (Figure 14a). Note that we
preserve the spectral contrast for all wavelengths < 550 nm, so our adjustment of k_{350} also implies a change at the
longer wavelengths, hence we simulate a different lidar ratio at 532 nm (Figure 14b). For our final set of optics, we
555 chose $k_{350} = 0.02$ to have a reasonable simulation of the OMI AI values that we discuss later in Section 3.4.2.

560 A new optics table was generated following the above three changes in assumptions of OA microphysical and
water uptake properties that we call “updated optics” throughout our figures and text. Now, we can revisit Figures
555 11b&c to understand the impact of this optics update on the model-simulated SSA comparisons with the in-situ and
4STAR observations. For the in-situ profile at 550 nm, there is a small decrease in model SSA with “OA-loss +
560 updated optics” compared to the “OA-loss” case (< 0.01), and it remains within 0.02 of the observed SSA value at all
altitudes (Figure 11b). Figure 11c is better at showing the impact of these changes on the broader spectral curve. The
“updated optics” case is less absorbing in the shortest 400 nm channel, but otherwise more absorbing than both the
baseline and “OA-loss with default optics” case. The former is expected due to the reduced OA absorption in near-
UV and latter is possibly due to the reduced hygroscopic growth assumptions that are leading to the formation of
565 effectively smaller particles at enhanced RH within the smoke plumes. However, overall, the “OA-loss+updated
optics” case shows the best agreement with the 4STAR observations compared to the other two cases for wavelengths
less than 700 nm (Table 3). At longer wavelengths the improvement is less clear; although “OA-loss + updated optics”
is closest to the 4STAR observations at 870 nm of all our experiment, it is the worst agreement at 1000 nm. We did
not investigate other aerosol components (e.g., dust) that could contribute to especially longer wavelength impacts.
570 Note that the results in Figure 11c are the average of three 4STAR retrievals on Sep 24, 2016 (Figure 3), but similar
SSA magnitudes and spectral curve shape, both for 4STAR and the different model simulations hold when we average
across all days of the ORACLES-I campaign (not shown here).

3.3 AOD and SSA Evaluation at Near-Source AERONET sites

575 We evaluated the model performance of AOD and SSA at all the AERONET sites depicted in Figure 1a. For
brevity, we present here the comparative results from two key near-source sites, Mongu_Inn and Lubango, that had
data availability for most days of September 2016 and are most contrasting in terms of the model performance. The
model shows good agreement with AERONET observations over Lubango in terms of both AOD and SSA, and the
final “OA-loss + updated optics” case has overall similar performance to the model baseline case (Figures 15a, c) and
improves the SSA simulation at 440 nm and 675 nm (Table 4). At Mongu_Inn on the other hand, the model appears
to have a systematic low bias compared to the AERONET observed AOD but nonetheless can capture its daily
variability (Figure 15b). For SSA at Mongu (Figure 15d), the model largely overestimates the absorption at longer
wavelengths, and this together with AOD underestimation suggests that the model is likely missing a contribution
580 from coarse-mode particles over this site. However, the model “OA-loss+updated optics” case here corrected for the
excessive absorption at the shortest AERONET channel compared to the baseline simulation.

580 **Table 4. Comparison of the AERONET and GEOS SSA at two AERONET locations during September 2016.**

Wavelength (nm)	Location	Monthly Mean SSA		
		AERONET observations	GEOS baseline	GEOS OA-loss+updated optics
440	Lubango	0.88	0.87	0.88
	Mongu_Inn	0.88	0.84	0.87
675	Lubango	0.87	0.88	0.86
	Mongu_Inn	0.86	0.85	0.84

3.4 Satellite Perspective: Impact of updated optics on AOD and AI

3.4.1 Comparisons with MODIS NNR AOD Retrievals

Satellite-based observations are used in this section to assess the model performance over the broader SE 585 Atlantic as well as the source region over southern and central Africa. Figure 16a shows the September 2016 monthly mean MODIS NNR AOD. We sample the model AOD based on the MODIS swath, overpass time, and data availability, and the resulting monthly mean AOD from the model baseline and the final “OA-loss+updated optics” 590 simulations are shown in Figures 16b, d, respectively. The last column (Figures 16c&e) shows the differences between the model and the observations. Broadly, as depicted in the AOD difference plots, both model simulations show a good agreement with the NNR retrievals, especially over the ocean and the smoke outflow region compared to the 595 source region over the continent. There is a significant underestimation in terms of model AOD over the south-east parts of the continent that persists in both the model simulations. This is a shortcoming of the GEOS model that has persisted in previous model versions as well, possibly due to missing biomass burning or coarse-mode aerosol sources 600 (Das et al. 2017). Otherwise, there is a high bias in the model AOD in the areas around the west coast and 10° S in the baseline simulation (Figure 16c). In our final simulation, however, this high bias in model AOD is reduced from +0.02 to -0.02 (Figures 16d&e). Closer to the burning sources over land, this decrease in model AOD in our final simulation 605 is due to the adjusted hygroscopic growth for the OA particles (see section 3.2), whereas over the ocean, as the plumes move away from the continental burning sources, the decrease in model AOD is due to the accounting of OA loss with increasing smoke age. Finally, we also present the performance metrics (mean bias, root-mean-square error or RMSE, and Pearson correlation coefficient or r) to quantify the agreement between the model simulations and the 610 observations with a focus over the ORACLES-I region (Figures 16c&e). The statistical comparisons further emphasize that inclusion of OA loss processes and adjustments to model OA optics does not deteriorate the model performance in terms of AOD simulation, instead makes it marginally better compared to baseline run by lowering the RMSE (from 0.11 to 0.08) and increasing the r values (from 0.91 to 0.93). Note that we chose to show only the Aqua MODIS results here since Aqua has a closer overpass time with OMI (Aura) than Terra, but the comparisons of model AOD 615 simulations with respect to Terra MODIS retrievals (not shown here) also showed similar results.

3.4.2 Comparisons with OMI AI Observations

In Figure 17 we show the GEOS-simulated OMI AI for September 2016 in comparison to the OMI retrievals. The OMI retrieved AI is shown in Figure 17a. To minimize the impact of clouds on the comparison we retain only 610 OMI pixels with QA = 0 (low probability of cloud contamination). For the model-calculated AI, the GEOS-simulated aerosol profiles are sampled at the OMI footprints. The model optical property assumptions are applied to the simulated aerosol profiles, and with the OMI observation geometry and retrieved surface reflectance are input to the AI calculator, which simulates the OMI radiances. The simulated radiances only include terms for the aerosol, molecular background, and surface.

Two cases are shown in the comparison: the GEOS baseline run (Figure 17b) and the final run that includes 615 OA loss with smoke age, increased biomass burning emissions, and ORACLES-informed optical properties for OA (“OA-loss+updated optics,” Figure 17d). The baseline run, with its more highly absorbing OA assumptions and high bias in aerosol loading especially near the coast of southwest Africa (10°S, Figure 16c) results in the model overestimating the AI relative to OMI, with this high bias especially apparent over both land and ocean where the

620 AOD was overestimated in the model (Figure 17c). By contrast, the GEOS model run with the ORACLES-informed adjustment to the optical property assumptions, along with the reduced overall burden of OA, results in a much more favorable comparison of the simulated to retrieved AI (Figure 17e). The apparent discontinuity in the AI magnitude between land and sea along the west coast of southern Africa is a sampling artifact brought on by cloud screening, with nearly 3x as many OMI pixels retained over land as for over the coastal ocean. For this reason, we restrict a quantitative assessment of the model performance to the boxed region over land shown in Figures 17c&e, and statistics are reported in the figure panels. In the indicated region there is an improvement in the bias of the modeled AI from +0.28 to -0.14 and a reduction in the RMSE from 0.42 to 0.30 in moving to the updated aerosol optics. This improvement and our assessment of the model performance with the independent OMI dataset shows the overall consistency between the in situ derived optical properties from the ORACLES measurements and what can be retrieved from space-based remote sensing, with the GEOS model as the interpolator between the two datasets.

630 3.5 Radiative Implications

635 Finally, we consider the impact of the updated aerosol simulation on the modeled direct radiative forcing of the aerosols, which along with any possible aerosol-cloud interactions drive the aerosol impacts on climate. Figure 18a shows the September 2016 monthly mean 550 nm AOD difference between the GEOS baseline and updated (OA-loss+updated optics) model runs. The difference is consistent with the results in Figure 16 and shows that the enhanced biomass burning emissions in the updated run result in a slightly higher AOD over southeastern Africa, while the inclusion of the OA loss process in the updated run leads to somewhat less aerosol downwind and an overall lower smoke AOD over the southeast Atlantic compared to the baseline (i.e., the baseline run has a higher AOD over the ocean). Clouds are not much changed between the two model runs, so in Figure 18b we show the low cloud fraction 640 from the baseline run, which shows a main cloud feature (cloud fraction > 40%) centered at 10° – 15°N extending west of the continent.

645 Figure 18c shows the TOA all-sky shortwave (SW) radiative forcing due to aerosol, presented as a difference between our two runs. For each model run, the radiative forcing is computed by two successive calls to the radiative transfer code, one including the effects of aerosols and the other without the aerosols. The aerosol forcing is defined as the difference between the net TOA radiation with aerosols minus the net TOA radiation without aerosols (i.e., $SW_{net_aer} - SW_{net_noaer}$) and represent an increase (positive) or decrease (negative) of energy. There is an overall $\sim 1 \text{ W m}^{-2}$ difference in the SW forcing over the southeast Atlantic on the north edge of the smoke plume. This difference is on the margins of the smoke plume to the north of the main cloud features (Figure 18b) and has a negative magnitude as defined because in the baseline simulation there is more (relatively cooling) aerosol over the darker ocean surface 650 and so more radiation reflected to space. The broad positive SW forcing difference over the continent reflects the relatively greater backscattered solar radiation over the dark continental surface corresponding to the higher AOD in that region in the updated model run (region of over-land negative AOD difference in Figure 18a).

655 Finally, Figure 18d shows the SW atmospheric heating due to aerosols in the two model runs. This is the difference in the net forcing at TOA and at the surface. That enhanced loading (Figure 18a) and the relatively more absorbing optics of the baseline suggest a greater warming of the atmosphere versus the updated run, which would tend to stabilize the atmosphere. By contrast, our updated simulation has somewhat less atmospheric warming over the regional cloud decks.

4 Conclusions and Future Directions

660 In this study, we utilized the detailed ORACLES-I aircraft observations to evaluate the current state of biomass burning aerosol properties and transport in the NASA GEOS model following recent developments in its representation of carbonaceous aerosols. An example case study of September 24 was analyzed in detail, during which in-situ and remote sensing observations showed a presence of multi-layered smoke plume structure with significantly varying SSA in the vertical. Our baseline simulations were not able to represent the observed OA:BC ratio nor the vertically varying single scattering albedo. Analyzing the simulated smoke age suggests that the higher altitude, less 665 absorbing smoke in the plume was younger (~ 4 days), while the lower altitude and more absorbing smoke plume was older (~ 7 days). We hypothesize a loss process—chemical or microphysical—to explain the change in aerosol absorption as the smoke plume ages, and we apply a simple 6-day e-folding loss rate to the hydrophilic biomass burning OA to simulate this process. Adding this loss channel requires some adjustment to the assumed aerosol emissions to approximately conserve the regional aerosol loading and further improve the simulated OA:BC ratio, and 670 accordingly we have increased our biomass burning emissions of OA by 60% and biomass burning BC emissions by 15%. Next, we use the aircraft-based observations to better constrain the simulation of aerosol optical properties. For

the biomass burning OA aerosol component within GEOS, we adjust the lognormal size distribution to have a modal radius, $r_n = 0.09 \mu\text{m}$ and $\sigma = 1.5$ based on the ORACLES-I HiGEAR (or UHSAS) observations. Secondly, the OA hygroscopic growth is assumed to increase less rapidly with increasing RH compared to default assumptions and simulate the hygroscopic growth rate of model BC, which provides a simulated $f(\text{RH})$ similar to the observed. Finally, we also adjusted the OA complex refractive index ($k_{350} = 0.02$) to reduce the OA absorption in the near-UV to match better with the HSRL-2 retrieved lidar ratio and OMI retrieved AI. Our final GEOS model simulation with additional OA loss and updated optics showed a better performance in simulating AOD and SSA compared to independent AERONET observations and MODIS NNR AOD retrievals for the entire month of September 2016. In terms of radiative implications of our model adjustments, the final GEOS simulation suggests a decreased atmospheric warming of $\sim 2 \text{ W m}^{-2}$ over the South-east Atlantic region and above the stratocumulus cloud decks compared to the model baseline simulations.

The simplistic approach presented in this study to address the microphysical or chemical loss of OA with increasing smoke age lacks a specific physical basis. In subsequent modeling studies, the mechanisms causing this OA loss can be further explored and if the OA loss is indeed associated with continued oxidation of OA during the aging of smoke, the loss can be parameterized as a function of oxidant fields in the model rather than assuming a single e-folding time to simulate the aerosol loss. Moreover, observations over other major biomass burning regions of the globe need to be analyzed to find if a similar variation in SSA is observed for aging plumes in those regions and a global parameterization for OA loss will need to be explored. Finally, we will also need to utilize the observations from subsequent years of ORACLES (i.e., 2017 and 2018) to confirm whether the suggested set of OA microphysical and hygroscopic assumptions in the model for the 2016 case are also able to capture the seasonal variability of smoke emissions in this region.

Code availability. The GEOS Earth System Model source code and the instructions for model build are available at <https://github.com/GEOS-ESM/GEOSgcm/> (Last accessed: 16 May 2023).

Data availability. The GEOS model outputs and MODIS NNR and OMI AI retrievals needed to reproduce the results described in this paper are publicly available for download at data.nasa.gov repository (<https://doi.org/10.25966/wc4c-ke45>, Das, 2023), see complete dataset citation under References section. The ORACLES data was obtained from their ESPO Data Archive: <https://espo.nasa.gov/oracles/archive/browse/oracles/id8>, last accessed: 22 March 2022. The AERONET AOD retrievals (version 3) and SSA inversion product were downloaded from <https://aeronet.gsfc.nasa.gov/>, last accessed: 24 April 2023.

Author contributions. SD and PRC conceptualized the modeling and analysis approach, performed the simulations, and wrote the manuscript. HB, SD, and PRC performed the model-data comparative analysis. PRC and SG performed the simulations of OMI AI and helped with the interpretations of the remote-sensing observational data. All authors contributed to the editing of the manuscript.

Competing interests. The authors declare that they have no conflict of interest.

Acknowledgements. We would like to acknowledge the NASA Earth Science Division and GEOS model developmental efforts at GMAO for their support. This work was supported by NASA's Aura Science Team award 19-AURAST-0014. The computing resources supporting this work were provided by the NASA High-End Computing (HEC) Program through the NASA Center for Climate Simulation (NCCS) at the Goddard Space Flight Center. The authors also gratefully acknowledge the NOAA Air Resources Laboratory (ARL) for the provision of the HYSPLIT transport and dispersion model used in this publication.

5 References

Akagi, S. K., Yokelson, R. J., Wiedinmyer, C., Alvarado, M. J., Reid, J. S., Karl, T., Crounse, J. D., and Wennberg, P. O.: Emission factors for open and domestic biomass burning for use in atmospheric models, *Atmos Chem Phys*, 11, 4039–4072, <https://doi.org/10.5194/acp-11-4039-2011>, 2011.

Anderson, T. L. and Ogren, J. A.: Determining Aerosol Radiative Properties Using the TSI 3563 Integrating Nephelometer, *Aerosol Science and Technology*, 29, 57–69, <https://doi.org/10.1080/02786829808965551>, 1998.

720 Andreae, M. O.: Emission of trace gases and aerosols from biomass burning – an updated assessment, *Atmos Chem Phys*, 19, 8523–8546, <https://doi.org/10.5194/acp-19-8523-2019>, 2019.

725 Bacmeister, J. T., Suarez, M. J., and Robertson, F. R.: Rain Reevaporation, Boundary Layer–Convection Interactions, and Pacific Rainfall Patterns in an AGCM, *J Atmos Sci*, 63, 3383–3403, [https://doi.org/https://doi.org/10.1175/JAS3791.1](https://doi.org/10.1175/JAS3791.1), 2006.

730 Bian, H., Chin, M., Hauglustaine, D. A., Schulz, M., Myhre, G., Bauer, S. E., Lund, M. T., Karydis, V. A., Kucsera, T. L., Pan, X., Pozzer, A., Skeie, R. B., Steenrod, S. D., Sudo, K., Tsigaridis, K., Tsimpidi, A. P., and Tsyro, S. G.: Investigation of global particulate nitrate from the AeroCom phase~III experiment, *Atmos Chem Phys*, 17, 12911–12940, <https://doi.org/10.5194/acp-17-12911-2017>, 2017.

735 Buchard, V., da Silva, A. M., Colarco, P. R., Darmenov, A., Randles, C. A., Govindaraju, R., Torres, O., Campbell, J., and Spurr, R.: Using the OMI aerosol index and absorption aerosol optical depth to evaluate the NASA MERRA Aerosol Reanalysis, *Atmos Chem Phys*, 15, 5743–5760, <https://doi.org/10.5194/acp-15-5743-2015>, 2015.

740 Burgos, M. A., Andrews, E., Titos, G., Benedetti, A., Bian, H., Buchard, V., Curci, G., Kipling, Z., Kirkevåg, A., Kokkola, H., Laakso, A., Letertre-Danczak, J., Lund, M. T., Matsui, H., Myhre, G., Randles, C., Schulz, M., van Noije, T., Zhang, K., Alados-Arboledas, L., Baltensperger, U., Jefferson, A., Sherman, J., Sun, J., Weingartner, E., and Zieger, P.: A global model–measurement evaluation of particle light scattering coefficients at elevated relative humidity, *Atmos Chem Phys*, 20, 10231–10258, <https://doi.org/10.5194/acp-20-10231-2020>, 2020.

745 Burton, S. P., Ferrare, R. A., Hostetler, C. A., Hair, J. W., Rogers, R. R., Oblean, M. D., Butler, C. F., Cook, A. L., Harper, D. B., and Froyd, K. D.: Aerosol classification using airborne High Spectral Resolution Lidar measurements – methodology and examples, *Atmos Meas Tech*, 5, 73–98, <https://doi.org/10.5194/amt-5-73-2012>, 2012.

750 Capes, G., Johnson, B., McFiggans, G., Williams, P. I., Haywood, J., and Coe, H.: Aging of biomass burning aerosols over West Africa: Aircraft measurements of chemical composition, microphysical properties, and emission ratios, *Journal of Geophysical Research: Atmospheres*, 113, [https://doi.org/https://doi.org/10.1029/2008JD009845](https://doi.org/10.1029/2008JD009845), 2008.

755 Chand, D., Wood, R., Anderson, T. L., Satheesh, S. K., and Charlson, R. J.: Satellite-derived direct radiative effect of aerosols dependent on cloud cover, *Nat Geosci*, 2, 181–184, <https://doi.org/10.1038/ngeo437>, 2009.

760 Chin, M., Ginoux, P., Kinne, S., Torres, O., Holben, B. N., Duncan, B. N., Martin, R. V., Logan, J. A., Higurashi, A., and Nakajima, T.: Tropospheric Aerosol Optical Thickness from the GOCART Model and Comparisons with Satellite and Sun Photometer Measurements, *J Atmos Sci*, 59, 461–483, [https://doi.org/https://doi.org/10.1175/1520-0469\(2002\)059<0461:TAOTFT>2.0.CO;2](https://doi.org/10.1175/1520-0469(2002)059<0461:TAOTFT>2.0.CO;2), 2002.

Christian, T. J., Kleiss, B., Yokelson, R. J., Holzinger, R., Crutzen, P. J., Hao, W. M., Saharjo, B. H., and Ward, D. E.: Comprehensive laboratory measurements of biomass-burning emissions: 1. Emissions from Indonesian, African, and other fuels, *Journal of Geophysical Research: Atmospheres*, 108, [https://doi.org/https://doi.org/10.1029/2003JD003704](https://doi.org/10.1029/2003JD003704), 2003.

765 Colarco, P., da Silva, A., Chin, M., and Diehl, T.: Online simulations of global aerosol distributions in the NASA GEOS-4 model and comparisons to satellite and ground-based aerosol optical depth, *Journal of Geophysical Research: Atmospheres*, 115, [https://doi.org/https://doi.org/10.1029/2009JD012820](https://doi.org/10.1029/2009JD012820), 2010.

770 Colarco, P. R., Nowottnick, E. P., Randles, C. A., Yi, B., Yang, P., Kim, K.-M., Smith, J. A., and Bardeen, C. G.: Impact of radiatively interactive dust aerosols in the NASA GEOS-5 climate model: Sensitivity to dust particle shape and refractive index, *Journal of Geophysical Research: Atmospheres*, 119, 753–786, [https://doi.org/https://doi.org/10.1002/2013JD020046](https://doi.org/10.1002/2013JD020046), 2014.

775 Colarco, P. R., Gassó, S., Ahn, C., Buchard, V., da Silva, A. M., and Torres, O.: Simulation of the Ozone Monitoring Instrument aerosol index using the NASA Goddard Earth Observing System aerosol reanalysis products, *Atmos Meas Tech*, 10, 4121–4134, <https://doi.org/10.5194/amt-10-4121-2017>, 2017.

780 Collow, A., Das, S., Colarco, P., da Silva, A., Miller, M., and Arnold, N.: Diagnosing Excessive Subsidence across the Southeast Atlantic in the Goddard Earth Observing System (GEOS), *Journal of Geophysical Research: Atmospheres*, *in preparation*.

770 Cubison, M. J., Ortega, A. M., Hayes, P. L., Farmer, D. K., Day, D., Lechner, M. J., Brune, W. H., Apel, E., Diskin, G. S., Fisher, J. A., Fuelberg, H. E., Hecobian, A., Knapp, D. J., Mikoviny, T., Riemer, D., Sachse, G. W., Sessions, W., Weber, R. J., Weinheimer, A. J., Wisthaler, A., and Jimenez, J. L.: Effects of aging on organic aerosol from open biomass burning smoke in aircraft and laboratory studies, *Atmos Chem Phys*, 11, 12049–12064, <https://doi.org/10.5194/acp-11-12049-2011>, 2011.

775 Darmenov, A. S., and Da Silva, A.: Technical Report Series on Global Modeling and Data Assimilation, Volume 38 The Quick Fire Emissions Dataset (QFED): Documentation of versions 2.1, 2.2 and 2.4 (Edited by R.D., Koster), 2015.

780 Das, S., Harshvardhan, H., Bian, H., Chin, M., Curci, G., Protonotariou, A. P., Mielonen, T., Zhang, K., Wang, H., and Liu, X.: Biomass burning aerosol transport and vertical distribution over the South African-Atlantic region, *Journal of Geophysical Research: Atmospheres*, 122, 6391–6415, <https://doi.org/https://doi.org/10.1002/2016JD026421>, 2017.

785 Das, S., Colarco, P. R., and Harshvardhan, H.: The Influence of Elevated Smoke Layers on Stratocumulus Clouds Over the SE Atlantic in the NASA Goddard Earth Observing System (GEOS) Model, *Journal of Geophysical Research: Atmospheres*, 125, e2019JD031209, <https://doi.org/https://doi.org/10.1029/2019JD031209>, 2020.

790 Das, S., Colarco, P., Bian, H., and Gasso, S.: Improved Simulations of Biomass Burning Aerosol Optical Properties and Lifetimes during the ORACLES-I Campaign: Results from the NASA GEOS Model, data.nasa.gov [data set], <https://doi.org/10.25966/wc4c-ke45>, 2023.

795 DeCarlo, P. F., Dunlea, E. J., Kimmel, J. R., Aiken, A. C., Sueper, D., Crounse, J., Wennberg, P. O., Emmons, L., Shinozuka, Y., Clarke, A., Zhou, J., Tomlinson, J., Collins, D. R., Knapp, D., Weinheimer, A. J., Montzka, D. D., Campos, T., and Jimenez, J. L.: Fast airborne aerosol size and chemistry measurements above Mexico City and Central Mexico during the MILAGRO campaign, *Atmos Chem Phys*, 8, 4027–4048, <https://doi.org/10.5194/acp-8-4027-2008>, 2008.

800 Dobrucki, A., Zuidema, P., Howell, S. G., Saide, P., Freitag, S., Aiken, A. C., Burton, S. P., Sedlacek III, A. J., Redemann, J., and Wood, R.: An attribution of the low single-scattering albedo of biomass burning aerosol over the southeastern Atlantic, *Atmos Chem Phys*, 23, 4775–4799, <https://doi.org/10.5194/acp-23-4775-2023>, 2023.

805 Doherty, S. J., Saide, P. E., Zuidema, P., Shinozuka, Y., Ferrada, G. A., Gordon, H., Mallet, M., Meyer, K., Painemal, D., Howell, S. G., Freitag, S., Dobrucki, A., Podolske, J. R., Burton, S. P., Ferrare, R. A., Howes, C., Nabat, P., Carmichael, G. R., da Silva, A., Pistone, K., Chang, I., Gao, L., Wood, R., and Redemann, J.: Modeled and observed properties related to the direct aerosol radiative effect of biomass burning aerosol over the southeastern Atlantic, *Atmos Chem Phys*, 22, 1–46, <https://doi.org/10.5194/acp-22-1-2022>, 2022.

810 Dubovik, O. and King, M. D.: A flexible inversion algorithm for retrieval of aerosol optical properties from Sun and sky radiance measurements, *Journal of Geophysical Research: Atmospheres*, 105, 20673–20696, <https://doi.org/https://doi.org/10.1029/2000JD900282>, 2000.

815 Forrister, H., Liu, J., Scheuer, E., Dibb, J., Ziembka, L., Thornhill, K. L., Anderson, B., Diskin, G., Perring, A. E., Schwarz, J. P., Campuzano-Jost, P., Day, D. A., Palm, B. B., Jimenez, J. L., Nenes, A., and Weber, R. J.: Evolution of brown carbon in wildfire plumes, *Geophys Res Lett*, 42, 4623–4630, <https://doi.org/https://doi.org/10.1002/2015GL063897>, 2015.

820 de Freitas, S. R., Grell, G., Molod, A., Thompson, M. A., Putman, W. M., e Silva, C. M. S., and de Souza, É. P.: Assessing the Grell-Freitas Convection Parameterization in the NASA GEOS Modeling System, *J Adv Model Earth Syst*, 10, 1266–1289, 2018.

825 Freney, E. J., Adachi, K., and Buseck, P. R.: Internally mixed atmospheric aerosol particles: Hygroscopic growth and light scattering, *Journal of Geophysical Research: Atmospheres*, 115, <https://doi.org/https://doi.org/10.1029/2009JD013558>, 2010.

830 Friedl, M. A., Sulla-Menashe, D., Tan, B., Schneider, A., Ramankutty, N., Sibley, A., and Huang, X.: MODIS Collection 5 global land cover: Algorithm refinements and characterization of new datasets, *Remote Sens Environ*, 114, 168–182, <https://doi.org/https://doi.org/10.1016/j.rse.2009.08.016>, 2010.

835 Gelaro, R., McCarty, W., Suárez, M. J., Todling, R., Molod, A., Takacs, L., Randles, C. A., Darmenov, A., Bosilovich, M. G., Reichle, R., Wargan, K., Coy, L., Cullather, R., Draper, C., Akella, S., Buchard, V., Conaty, A., da Silva,

820 A. M., Gu, W., Kim, G.-K., Koster, R., Lucchesi, R., Merkova, D., Nielsen, J. E., Partyka, G., Pawson, S., Putman, W., Rienerer, M., Schubert, S. D., Sienkiewicz, M., and Zhao, B.: The Modern-Era Retrospective Analysis for Research and Applications, Version 2 (MERRA-2), *J. Clim.*, 30, 5419–5454, [https://doi.org/https://doi.org/10.1175/JCLI-D-16-0758.1](https://doi.org/10.1175/JCLI-D-16-0758.1), 2017.

825 Giles, D. M., Sinyuk, A., Sorokin, M. G., Schafer, J. S., Smirnov, A., Slutsker, I., Eck, T. F., Holben, B. N., Lewis, J. R., Campbell, J. R., Welton, E. J., Korkin, S. V., and Lyapustin, A. I.: Advancements in the Aerosol Robotic Network (AERONET) Version~3 database – automated near-real-time quality control algorithm with improved cloud screening for Sun photometer aerosol optical depth (AOD) measurements, *Atmos. Meas. Tech.*, 12, 169–209, <https://doi.org/10.5194/amt-12-169-2019>, 2019.

Gordon, H., Field, P. R., Abel, S. J., Dalvi, M., Grosvenor, D. P., Hill, A. A., Johnson, B. T., Miltenberger, A. K., Yoshioka, M., and Carslaw, K. S.: Large simulated radiative effects of smoke in the south-east Atlantic, *Atmos. Chem. Phys.*, 18, 15261–15289, <https://doi.org/10.5194/acp-18-15261-2018>, 2018.

830 de Graaf, M., Schulte, R., Peers, F., Waquet, F., Tilstra, L. G., and Stammes, P.: Comparison of south-east Atlantic aerosol direct radiative effect over clouds from SCIAMACHY, POLDER and OMI–MODIS, *Atmos. Chem. Phys.*, 20, 6707–6723, <https://doi.org/10.5194/acp-20-6707-2020>, 2020.

Grell, G. A. and Freitas, S. R.: A scale and aerosol aware stochastic convective parameterization for weather and air quality modeling, *Atmos. Chem. Phys.*, 14, 5233–5250, <https://doi.org/10.5194/acp-14-5233-2014>, 2014.

835 Hair, J. W., Hostetler, C. A., Cook, A. L., Harper, D. B., Ferrare, R. A., Mack, T. L., Welch, W., Izquierdo, L. R., and Hovis, F. E.: Airborne High Spectral Resolution Lidar for profiling aerosol optical properties, *Appl. Opt.*, 47, 6734–6752, <https://doi.org/10.1364/AO.47.006734>, 2008.

840 Hersbach, H., Bell, B., Berrisford, P., Hirahara, S., Horányi, A., Muñoz-Sabater, J., Nicolas, J., Peubey, C., Radu, R., Schepers, D., Simmons, A., Soci, C., Abdalla, S., Abellán, X., Balsamo, G., Bechtold, P., Biavati, G., Bidlot, J., Bonavita, M., De Chiara, G., Dahlgren, P., Dee, D., Diamantakis, M., Dragani, R., Flemming, J., Forbes, R., Fuentes, M., Geer, A., Haimberger, L., Healy, S., Hogan, R. J., Hólm, E., Janisková, M., Keeley, S., Laloyaux, P., Lopez, P., Lupu, C., Radnoti, G., de Rosnay, P., Rozum, I., Vamborg, F., Villaume, S., and Thépaut, J.-N.: The ERA5 global reanalysis, *Quarterly Journal of the Royal Meteorological Society*, 146, 1999–2049, [https://doi.org/https://doi.org/10.1002/qj.3803](https://doi.org/10.1002/qj.3803), 2020.

845 Hess, M., Koepke, P., and Schult, I.: Optical Properties of Aerosols and Clouds: The Software Package OPAC, *Bull. Am. Meteorol. Soc.*, 79, 831–844, [https://doi.org/https://doi.org/10.1175/1520-0477\(1998\)079<0831:OPOAAC>2.0.CO;2](https://doi.org/10.1175/1520-0477(1998)079<0831:OPOAAC>2.0.CO;2), 1998.

850 Hodzic, A., Campuzano-Jost, P., Bian, H., Chin, M., Colarco, P. R., Day, D. A., Froyd, K. D., Heinold, B., Jo, D. S., Katich, J. M., Kodros, J. K., Nault, B. A., Pierce, J. R., Ray, E., Schacht, J., Schill, G. P., Schroder, J. C., Schwarz, J. P., Sueper, D. T., Tegen, I., Tilmes, S., Tsigaridis, K., Yu, P., and Jimenez, J. L.: Characterization of organic aerosol across the global remote troposphere: a comparison of ATom measurements and global chemistry models, *Atmos. Chem. Phys.*, 20, 4607–4635, <https://doi.org/10.5194/acp-20-4607-2020>, 2020.

855 Holben, B. N., Eck, T. F., Slutsker, I., Tanré, D., Buis, J. P., Setzer, A., Vermote, E., Reagan, J. A., Kaufman, Y. J., Nakajima, T., Lavenu, F., Jankowiak, I., and Smirnov, A.: AERONET—A Federated Instrument Network and Data Archive for Aerosol Characterization, *Remote Sens. Environ.*, 66, 1–16, [https://doi.org/https://doi.org/10.1016/S0034-4257\(98\)00031-5](https://doi.org/10.1016/S0034-4257(98)00031-5), 1998.

Howell, S. G., Clarke, A. D., Shinozuka, Y., Kapustin, V., McNaughton, C. S., Huebert, B. J., Doherty, S. J., and Anderson, T. L.: Influence of relative humidity upon pollution and dust during ACE-Asia: Size distributions and implications for optical properties, *Journal of Geophysical Research: Atmospheres*, 111, [https://doi.org/https://doi.org/10.1029/2004JD005759](https://doi.org/10.1029/2004JD005759), 2006.

860 Iacono, M. J., Delamere, J. S., Mlawer, E. J., Shephard, M. W., Clough, S. A., and Collins, W. D.: Radiative forcing by long-lived greenhouse gases: Calculations with the AER radiative transfer models, *Journal of Geophysical Research: Atmospheres*, 113, [https://doi.org/https://doi.org/10.1029/2008JD009944](https://doi.org/10.1029/2008JD009944), 2008.

865 Jolleys, M. D., Coe, H., McFiggans, G., Capes, G., Allan, J. D., Crosier, J., Williams, P. I., Allen, G., Bower, K. N., Jimenez, J. L., Russell, L. M., Grutter, M., and Baumgardner, D.: Characterizing the Aging of Biomass Burning Organic Aerosol by Use of Mixing Ratios: A Meta-analysis of Four Regions, *Environ. Sci. Technol.*, 46, 13093–13102, <https://doi.org/10.1021/es302386v>, 2012.

870 Kacenelenbogen, M. S., Vaughan, M. A., Redemann, J., Young, S. A., Liu, Z., Hu, Y., Omar, A. H., LeBlanc, S., Shinozuka, Y., Livingston, J., Zhang, Q., and Powell, K. A.: Estimations of global shortwave direct aerosol radiative effects above opaque water clouds using a combination of A-Train satellite sensors, *Atmos Chem Phys*, 19, 4933–4962, <https://doi.org/10.5194/acp-19-4933-2019>, 2019.

Keil, A. and Haywood, J. M.: Solar radiative forcing by biomass burning aerosol particles during SAFARI 2000: A case study based on measured aerosol and cloud properties, *Journal of Geophysical Research: Atmospheres*, 108, [https://doi.org/https://doi.org/10.1029/2002JD002315](https://doi.org/10.1029/2002JD002315), 2003.

875 Kim, P. S., Jacob, D. J., Fisher, J. A., Travis, K., Yu, K., Zhu, L., Yantosca, R. M., Sulprizio, M. P., Jimenez, J. L., Campuzano-Jost, P., Froyd, K. D., Liao, J., Hair, J. W., Fenn, M. A., Butler, C. F., Wagner, N. L., Gordon, T. D., Welti, A., Wennberg, P. O., Crounse, J. D., St. Clair, J. M., Teng, A. P., Millet, D. B., Schwarz, J. P., Markovic, M. Z., and Perring, A. E.: Sources, seasonality, and trends of southeast US aerosol: an integrated analysis of surface, aircraft, and satellite observations with the GEOS-Chem chemical transport model, *Atmos Chem Phys*, 15, 10411–10433, <https://doi.org/10.5194/acp-15-10411-2015>, 2015.

880 Koster, R. D., Suarez, M. J., Ducharne, A., Stieglitz, M., and Kumar, P.: A catchment-based approach to modeling land surface processes in a general circulation model: 1. Model structure, *Journal of Geophysical Research: Atmospheres*, 105, 24809–24822, [https://doi.org/https://doi.org/10.1029/2000JD900327](https://doi.org/10.1029/2000JD900327), 2000.

885 Kroll, J. H., Smith, J. D., Che, D. L., Kessler, S. H., Worsnop, D. R., and Wilson, K. R.: Measurement of fragmentation and functionalization pathways in the heterogeneous oxidation of oxidized organic aerosol, *Phys. Chem. Chem. Phys.*, 11, 8005–8014, <https://doi.org/10.1039/B905289E>, 2009.

Lana, A., Bell, T. G., Simó, R., Vallina, S. M., Ballabrera-Poy, J., Kettle, A. J., Dachs, J., Bopp, L., Saltzman, E. S., Stefels, J., Johnson, J. E., and Liss, P. S.: An updated climatology of surface dimethylsulfide concentrations and emission fluxes in the global ocean, *Global Biogeochem Cy*, 25, n/a-n/a, <https://doi.org/10.1029/2010gb003850>, 2011.

890 LeBlanc, S. E., Redemann, J., Flynn, C., Pistone, K., Kacenelenbogen, M., Segal-Rosenheimer, M., Shinozuka, Y., Dunagan, S., Dahlgren, R. P., Meyer, K., Podolske, J., Howell, S. G., Freitag, S., Small-Griswold, J., Holben, B., Diamond, M., Wood, R., Formenti, P., Piketh, S., Maggs-Kölling, G., Gerber, M., and Namwoonde, A.: Above-cloud aerosol optical depth from airborne observations in the southeast Atlantic, *Atmos Chem Phys*, 20, 1565–1590, <https://doi.org/10.5194/acp-20-1565-2020>, 2020.

895 Levelt, P. F., Van Den Oord, G. H. J., Dobber, M. R., Mälkki, A., Visser, H., De Vries, J., Stammes, P., Lundell, J. O. V., and Saari, H.: The ozone monitoring instrument, *IEEE Transactions on Geoscience and Remote Sensing*, 44, 1093–1100, <https://doi.org/10.1109/TGRS.2006.872333>, 2006.

900 Levy, R. C., Mattoo, S., Munchak, L. A., Remer, L. A., Sayer, A. M., Patadia, F., and Hsu, N. C.: The Collection 6 MODIS aerosol products over land and ocean, *Atmos Meas Tech*, 6, 2989–3034, <https://doi.org/10.5194/amt-6-2989-2013>, 2013.

Lock, A. P., Brown, A. R., Bush, M. R., Martin, G. M., and Smith, R. N. B.: A New Boundary Layer Mixing Scheme. Part I: Scheme Description and Single-Column Model Tests, *Mon Weather Rev*, 128, 3187–3199, [https://doi.org/https://doi.org/10.1175/1520-0493\(2000\)128<3187:ANBLMS>2.0.CO;2](https://doi.org/10.1175/1520-0493(2000)128<3187:ANBLMS>2.0.CO;2), 2000.

905 Lu, Z., Liu, X., Zhang, Z., Zhao, C., Meyer, K., Rajapakshe, C., Wu, C., Yang, Z., and Penner, J. E.: Biomass smoke from southern Africa can significantly enhance the brightness of stratocumulus over the southeastern Atlantic Ocean, *Proceedings of the National Academy of Sciences*, 115, 2924–2929, <https://doi.org/10.1073/pnas.1713703115>, 2018.

Mallet, M., Nabat, P., Johnson, B., Michou, M., Haywood, J. M., Chen, C., and Dubovik, O.: Climate models generally underrepresent the warming by Central Africa biomass-burning aerosols over the Southeast Atlantic, *Sci Adv*, 7, eabg9998, <https://doi.org/10.1126/sciadv.abg9998>, 2021.

910 May, A. A., Lee, T., McMeeking, G. R., Akagi, S., Sullivan, A. P., Urbanski, S., Yokelson, R. J., and Kreidenweis, S. M.: Observations and analysis of organic aerosol evolution in some prescribed fire smoke plumes, *Atmos Chem Phys*, 15, 6323–6335, <https://doi.org/10.5194/acp-15-6323-2015>, 2015.

915 Meng, Z., Yang, P., Kattawar, G. W., Bi, L., Liou, K. N., and Laszlo, I.: Single-scattering properties of tri-axial ellipsoidal mineral dust aerosols: A database for application to radiative transfer calculations, *J Aerosol Sci*, 41, 501–512, [https://doi.org/https://doi.org/10.1016/j.jaerosci.2010.02.008](https://doi.org/10.1016/j.jaerosci.2010.02.008), 2010.

920 Myhre, G., Samset, B. H., Schulz, M., Balkanski, Y., Bauer, S., Berntsen, T. K., Bian, H., Bellouin, N., Chin, M., Diehl, T., Easter, R. C., Feichter, J., Ghan, S. J., Hauglustaine, D., Iversen, T., Kinne, S., Kirkevåg, A., Lamarque, J.-F., Lin, G., Liu, X., Lund, M. T., Luo, G., Ma, X., van Noije, T., Penner, J. E., Rasch, P. J., Ruiz, A., Seland, Ø., Skeie, R. B., Stier, P., Takemura, T., Tsigaridis, K., Wang, P., Wang, Z., Xu, L., Yu, H., Yu, F., Yoon, J.-H., Zhang, K., Zhang, H., and Zhou, C.: Radiative forcing of the direct aerosol effect from AeroCom Phase II simulations, *Atmos Chem Phys*, 13, 1853–1877, <https://doi.org/10.5194/acp-13-1853-2013>, 2013.

925 Nielsen, J. E., Pawson, S., Molod, A., Auer, B., da Silva, A. M., Douglass, A. R., Duncan, B., Liang, Q., Manyin, M., Oman, L. D., Putman, W., Strahan, S. E., and Wargan, K.: Chemical Mechanisms and Their Applications in the Goddard Earth Observing System (GEOS) Earth System Model, *J Adv Model Earth Syst*, 9, 3019–3044, [https://doi.org/https://doi.org/10.1002/2017MS001011](https://doi.org/10.1002/2017MS001011), 2017.

Park, S. and Bretherton, C. S.: The University of Washington Shallow Convection and Moist Turbulence Schemes and Their Impact on Climate Simulations with the Community Atmosphere Model, *J Clim*, 22, 3449–3469, [https://doi.org/https://doi.org/10.1175/2008JCLI2557.1](https://doi.org/10.1175/2008JCLI2557.1), 2009.

930 Pistone, K., Redemann, J., Doherty, S., Zuidema, P., Burton, S., Cairns, B., Cochrane, S., Ferrare, R., Flynn, C., Freitag, S., Howell, S. G., Kacenelenbogen, M., LeBlanc, S., Liu, X., Schmidt, K. S., Sedlacek III, A. J., Segal-Rozenhaimer, M., Shinozuka, Y., Starnes, S., van Diedenhoven, B., Van Harten, G., and Xu, F.: Intercomparison of biomass burning aerosol optical properties from in situ and remote-sensing instruments in ORACLES-2016, *Atmos Chem Phys*, 19, 9181–9208, <https://doi.org/10.5194/acp-19-9181-2019>, 2019.

935 Provencal, R., Gupta, M., Owano, T. G., Baer, D. S., Ricci, K. N., O'Keefe, A., and Podolske, J. R.: Cavity-enhanced quantum-cascade laser-based instrument for carbon monoxide measurements, *Appl. Opt.*, 44, 6712–6717, <https://doi.org/10.1364/AO.44.006712>, 2005.

Putman, W. M. and Lin, S.-J.: Finite-volume transport on various cubed-sphere grids, *J Comput Phys*, 227, 55–78, [https://doi.org/https://doi.org/10.1016/j.jcp.2007.07.022](https://doi.org/10.1016/j.jcp.2007.07.022), 2007.

940 Randles, C. A., da Silva, A. M., Buchard, V., Colarco, P. R., Darmenov, A., Govindaraju, R., Smirnov, A., Holben, B., Ferrare, R., Hair, J., Shinozuka, Y., and Flynn, C. J.: The MERRA-2 Aerosol Reanalysis, 1980 Onward. Part I: System Description and Data Assimilation Evaluation, *J Clim*, 30, 6823–6850, [https://doi.org/https://doi.org/10.1175/JCLI-D-16-0609.1](https://doi.org/10.1175/JCLI-D-16-0609.1), 2017.

945 Redemann, J., Wood, R., Zuidema, P., Doherty, S. J., Luna, B., LeBlanc, S. E., Diamond, M. S., Shinozuka, Y., Chang, I. Y., Ueyama, R., Pfister, L., Ryoo, J.-M., Dobrakci, A. N., da Silva, A. M., Longo, K. M., Kacenelenbogen, M. S., Flynn, C. J., Pistone, K., Knox, N. M., Piketh, S. J., Haywood, J. M., Formenti, P., Mallet, M., Stier, P., Ackerman, A. S., Bauer, S. E., Fridlind, A. M., Carmichael, G. R., Saide, P. E., Ferrada, G. A., Howell, S. G., Freitag, S., Cairns, B., Holben, B. N., Knobelspiesse, K. D., Tanelli, S., L'Ecuyer, T. S., Dzambo, A. M., Sy, O. O., McFarquhar, G. M., Poellot, M. R., Gupta, S., O'Brien, J. R., Nenes, A., Kacarab, M., Wong, J. P. S., Small-Griswold, J. D., Thornhill, K. L., Noone, D., Podolske, J. R., Schmidt, K. S., Pilewskie, P., Chen, H., Cochrane, S. P., Sedlacek, A. J., Lang, T. J., Stith, E., Segal-Rozenhaimer, M., Ferrare, R. A., Burton, S. P., Hostetler, C. A., Diner, D. J., Seidel, F. C., Platnick, S. E., Myers, J. S., Meyer, K. G., Spangenberg, D. A., Maring, H., and Gao, L.: An overview of the ORACLES (ObseRvations of Aerosols above CLouds and their intEractionS) project: aerosol–cloud–radiation interactions in the southeast Atlantic basin, *Atmos Chem Phys*, 21, 1507–1563, <https://doi.org/10.5194/acp-21-1507-2021>, 2021.

Rolph, G., Stein, A., and Stunder, B.: Real-time Environmental Applications and Display sYstem: READY, Environmental Modelling & Software, 95, 210–228, [https://doi.org/https://doi.org/10.1016/j.envsoft.2017.06.025](https://doi.org/10.1016/j.envsoft.2017.06.025), 2017.

950 Saide, P. E., Thompson, G., Eidhammer, T., da Silva, A. M., Pierce, R. B., and Carmichael, G. R.: Assessment of biomass burning smoke influence on environmental conditions for multiyear tornado outbreaks by combining aerosol-aware microphysics and fire emission constraints, *Journal of Geophysical Research: Atmospheres*, 121, 10, 210–294, 311, [https://doi.org/https://doi.org/10.1002/2016JD025056](https://doi.org/10.1002/2016JD025056), 2016.

965 Schulz, M., Textor, C., Kinne, S., Balkanski, Y., Bauer, S., Berntsen, T., Berglen, T., Boucher, O., Dentener, F., Guibert, S., Isaksen, I. S. A., Iversen, T., Koch, D., Kirkevåg, A., Liu, X., Montanaro, V., Myhre, G., Penner, J. E., Pitari, G., Reddy, S., Seland, Ø., Stier, P., and Takemura, T.: Radiative forcing by aerosols as derived from the AeroCom present-day and pre-industrial simulations, *Atmos Chem Phys*, 6, 5225–5246, <https://doi.org/10.5194/acp-6-5225-2006>, 2006.

970 Schwarz, J. P., Gao, R. S., Fahey, D. W., Thomson, D. S., Watts, L. A., Wilson, J. C., Reeves, J. M., Darbeheshi, M., Baumgardner, D. G., Kok, G. L., Chung, S. H., Schulz, M., Hendricks, J., Lauer, A., Kärcher, B., Slowik, J. G., Rosenlof, K. H., Thompson, T. L., Langford, A. O., Loewenstein, M., and Aikin, K. C.: Single-particle measurements of midlatitude black carbon and light-scattering aerosols from the boundary layer to the lower stratosphere, *Journal of Geophysical Research: Atmospheres*, 111, [https://doi.org/https://doi.org/10.1029/2006JD007076](https://doi.org/10.1029/2006JD007076), 2006.

975 Shinozuka, Y., Saide, P. E., Ferrada, G. A., Burton, S. P., Ferrare, R., Doherty, S. J., Gordon, H., Longo, K., Mallet, M., Feng, Y., Wang, Q., Cheng, Y., Dobrucki, A., Freitag, S., Howell, S. G., LeBlanc, S., Flynn, C., Segal-Rosenheimer, M., Pistone, K., Podolske, J. R., Stith, E. J., Bennett, J. R., Carmichael, G. R., da Silva, A., Govindaraju, R., Leung, R., Zhang, Y., Pfister, L., Ryoo, J.-M., Redemann, J., Wood, R., and Zuidema, P.: Modeling the smoky troposphere of the southeast Atlantic: a comparison to ORACLES airborne observations from September of 2016, *Atmos Chem Phys*, 20, 11491–11526, <https://doi.org/10.5194/acp-20-11491-2020>, 2020.

980 Shrivastava, M., Cappa, C. D., Fan, J., Goldstein, A. H., Guenther, A. B., Jimenez, J. L., Kuang, C., Laskin, A., Martin, S. T., Ng, N. L., Petaja, T., Pierce, J. R., Rasch, P. J., Roldin, P., Seinfeld, J. H., Shilling, J., Smith, J. N., Thornton, J. A., Volkamer, R., Wang, J., Worsnop, D. R., Zaveri, R. A., Zelenyuk, A., and Zhang, Q.: Recent advances in understanding secondary organic aerosol: Implications for global climate forcing, *Reviews of Geophysics*, 55, 509–559, [https://doi.org/https://doi.org/10.1002/2016RG000540](https://doi.org/10.1002/2016RG000540), 2017.

985 Sinyuk, A., Holben, B. N., Eck, T. F., Giles, D. M., Slutsker, I., Korkin, S., Schafer, J. S., Smirnov, A., Sorokin, M., and Lyapustin, A.: The AERONET Version 3 aerosol retrieval algorithm, associated uncertainties and comparisons to Version 2, *Atmos Meas Tech*, 13, 3375–3411, <https://doi.org/10.5194/amt-13-3375-2020>, 2020.

990 Stein, A. F., Draxler, R. R., Rolph, G. D., Stunder, B. J. B., Cohen, M. D., and Ngan, F.: NOAA's HYSPLIT Atmospheric Transport and Dispersion Modeling System, *Bull Am Meteorol Soc*, 96, 2059–2077, <https://doi.org/https://doi.org/10.1175/BAMS-D-14-00110.1>, 2015.

995 Stephens, M., Turner, N., and Sandberg, J.: Particle identification by laser-induced incandescence in a solid-state laser cavity, *Appl. Opt.*, 42, 3726–3736, <https://doi.org/10.1364/AO.42.003726>, 2003.

Strode, S. A., Ziemke, J. R., Oman, L. D., Lamsal, L. N., Olsen, M. A., and Liu, J.: Global changes in the diurnal cycle of surface ozone, *Atmos Environ*, 199, 323–333, <https://doi.org/https://doi.org/10.1016/j.atmosenv.2018.11.028>, 2019.

1000 Torres, O., Tanskanen, A., Veihelmann, B., Ahn, C., Braak, R., Bhartia, P. K., Veefkind, P., and Levelt, P.: Aerosols and surface UV products from Ozone Monitoring Instrument observations: An overview, *Journal of Geophysical Research: Atmospheres*, 112, [https://doi.org/https://doi.org/10.1029/2007JD008809](https://doi.org/10.1029/2007JD008809), 2007.

Tyson, P.D., Garstang, M., Swap, R., Källberg, P. and Edwards, M.: An Air Transport Climatology for Subtropical Southern Africa, *Int. J. Climatol.*, 16: 265-291. [https://doi.org/10.1002/\(SICI\)1097-0088\(199603\)16:3<265::AID-JOC8>3.0.CO;2-M](https://doi.org/10.1002/(SICI)1097-0088(199603)16:3<265::AID-JOC8>3.0.CO;2-M), 1996.

1005 Vakkari, V., Beukes, J. P., Dal Maso, M., Aurela, M., Josipovic, M., and van Zyl, P. G.: Major secondary aerosol formation in southern African open biomass burning plumes, *Nat Geosci*, 11, 580–583, <https://doi.org/10.1038/s41561-018-0170-0>, 2018.

1010 Veselovskii, I., Hu, Q., Goloub, P., Podvin, T., Korenskiy, M., Derimian, Y., Legrand, M., and Castellanos, P.: Variability in lidar-derived particle properties over West Africa due to changes in absorption: towards an understanding, *Atmos Chem Phys*, 20, 6563–6581, <https://doi.org/10.5194/acp-20-6563-2020>, 2020.

1015 Virkkula, A.: Correction of the Calibration of the 3-wavelength Particle Soot Absorption Photometer (3 λ PSAP),
Aerosol Science and Technology, 44, 706–712, <https://doi.org/10.1080/02786826.2010.482110>, 2010.

Wilcox, E. M.: Direct and semi-direct radiative forcing of smoke aerosols over clouds, Atmos Chem Phys, 12, 139–
149, <https://doi.org/10.5194/acp-12-139-2012>, 2012.

Wong, J. P. S., Nenes, A., and Weber, R. J.: Changes in Light Absorptivity of Molecular Weight Separated Brown
Carbon Due to Photolytic Aging, Environ Sci Technol, 51, 8414–8421, <https://doi.org/10.1021/acs.est.7b01739>,
2017.

1020 Yokelson, R. J., Crounse, J. D., DeCarlo, P. F., Karl, T., Urbanski, S., Atlas, E., Campos, T., Shinozuka, Y., Kapustin,
V., Clarke, A. D., Weinheimer, A., Knapp, D. J., Montzka, D. D., Holloway, J., Weibring, P., Flocke, F., Zheng,
W., Toohey, D., Wennberg, P. O., Wiedinmyer, C., Mauldin, L., Fried, A., Richter, D., Walega, J., Jimenez, J.
L., Adachi, K., Buseck, P. R., Hall, S. R., and Shetter, R.: Emissions from biomass burning in the Yucatan,
Atmos Chem Phys, 9, 5785–5812, <https://doi.org/10.5194/acp-9-5785-2009>, 2009.

1025 Zhang, J. and Reid, J. S.: MODIS aerosol product analysis for data assimilation: Assessment of over-ocean level 2
aerosol optical thickness retrievals, J Geophys Res Atmospheres 1984 2012, 111, D22207,
<https://doi.org/10.1029/2005jd006898>, 2006.

Zhang, Z., Meyer, K., Yu, H., Platnick, S., Colarco, P., Liu, Z., and Oreopoulos, L.: Shortwave direct radiative effects
of above-cloud aerosols over global oceans derived from 8~years of CALIOP and MODIS observations, Atmos
Chem Phys, 16, 2877–2900, <https://doi.org/10.5194/acp-16-2877-2016>, 2016.

1030 Zhao, R., Lee, A. K. Y., Huang, L., Li, X., Yang, F., and Abbatt, J. P. D.: Photochemical processing of aqueous
atmospheric brown carbon, Atmos Chem Phys, 15, 6087–6100, <https://doi.org/10.5194/acp-15-6087-2015>,
2015.

1035 Zhou, S., Collier, S., Jaffe, D. A., Briggs, N. L., Hee, J., Sedlacek III, A. J., Kleinman, L., Onasch, T. B., and Zhang,
Q.: Regional influence of wildfires on aerosol chemistry in the western US and insights into atmospheric aging
of biomass burning organic aerosol, Atmos Chem Phys, 17, 2477–2493, <https://doi.org/10.5194/acp-17-2477-2017>, 2017.

6 List of Figures

1040

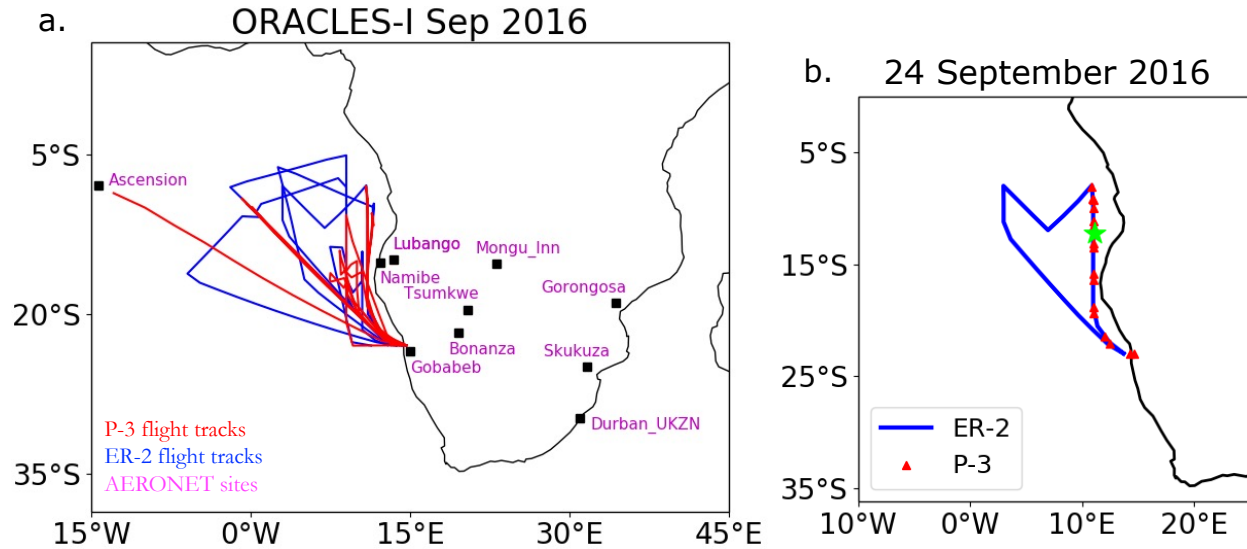


Figure 1. (a) Location of ORACLES-I P-3 and ER-2 flights off southwestern Africa during September 2016 and ground-based AERONET sites over the continent. (b) P-3 and ER-2 flight tracks for September 24, 2016, with the green star highlighting the location of the vertical profile illustrated in later plots.

1045

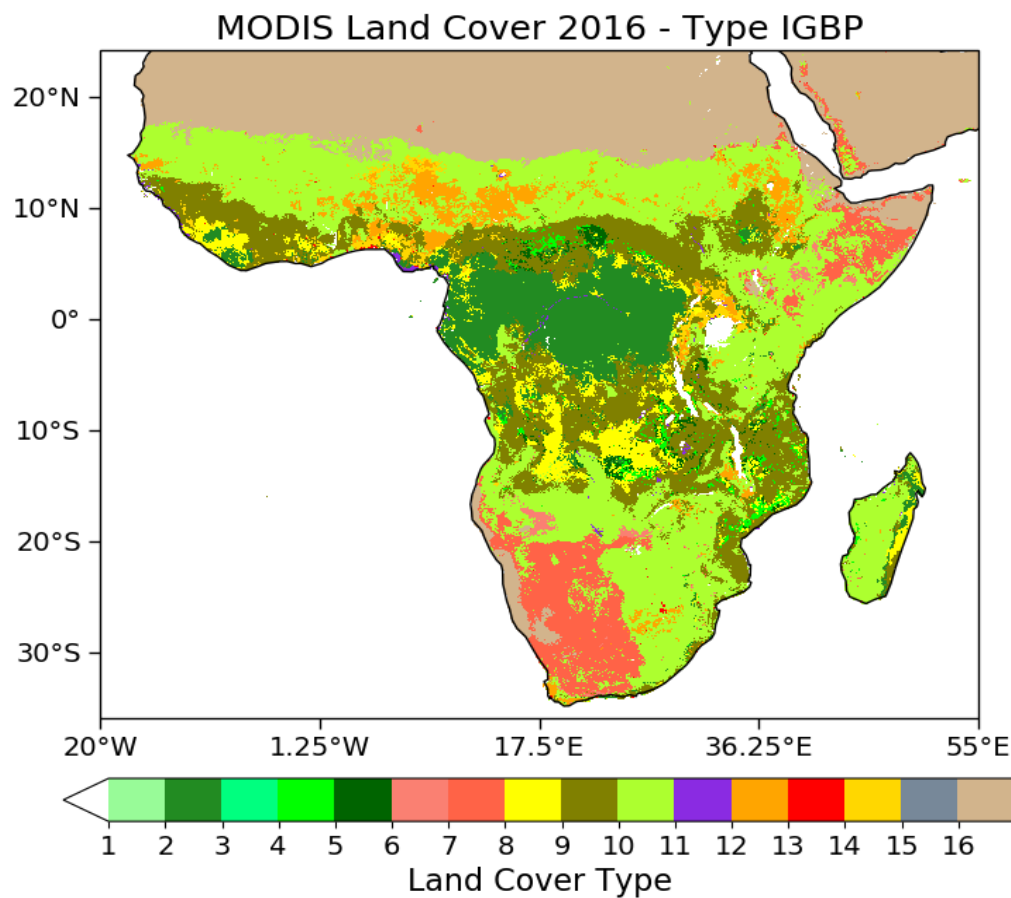


Figure 2. Land cover or vegetation types for 2016 from the MODIS Land Cover Type Product (MCD12C1) using the IGBP classification scheme.

1050

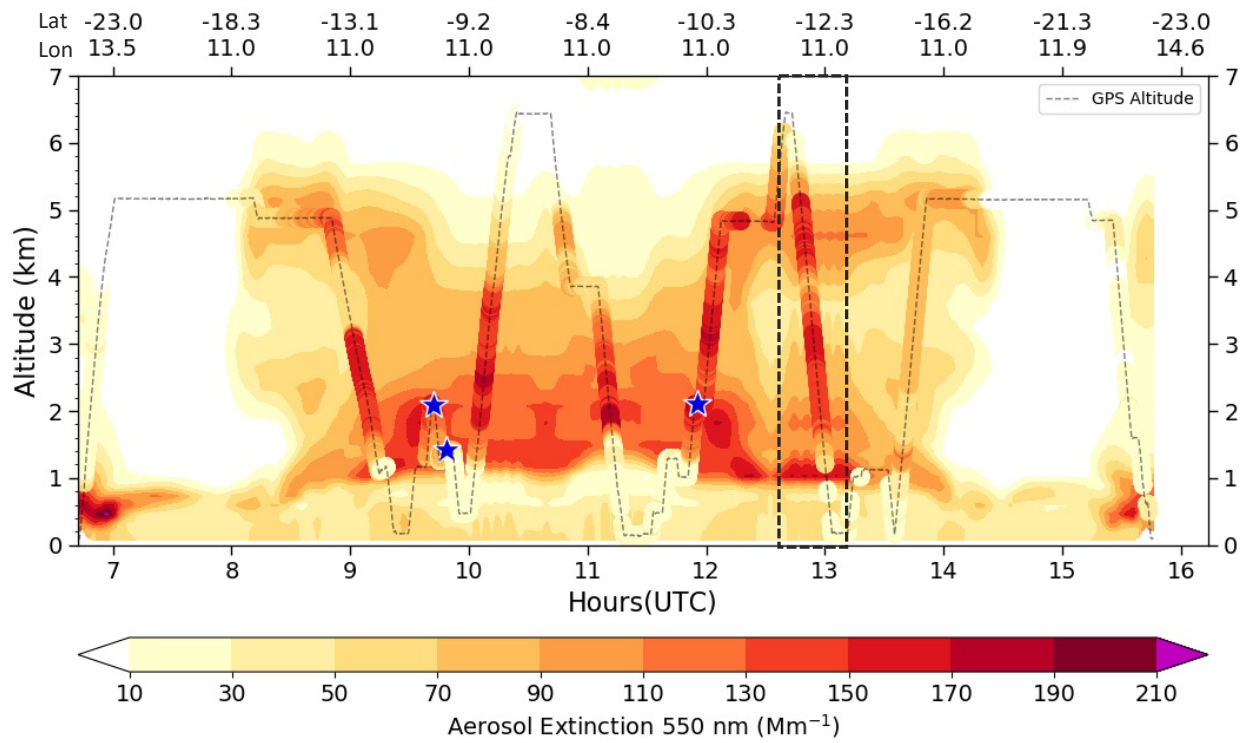
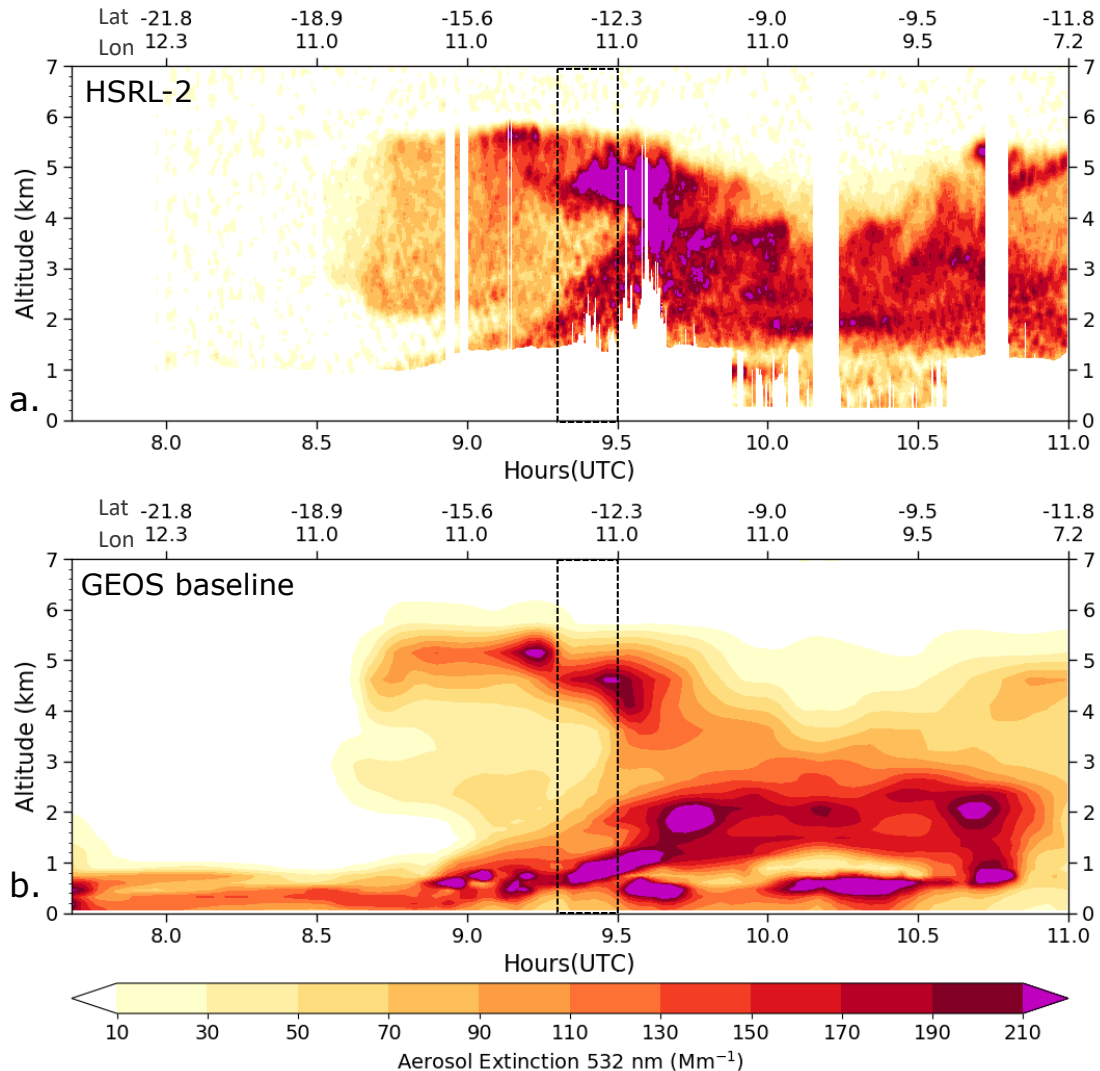


Figure 3. Background is the 550 nm extinction profile simulated in the GEOS baseline run along the P-3 flight track on September 24, 2016. Overplotted are the P-3 measured extinction values. Dashed gray line shows the P-3 flown altitude profile along the track. Dashed black box centered at 13 UTC shows the location of the specific profile highlighted by the green star in Figure 1b and analyzed in later plots. Blue stars are the locations of specific 4STAR SSA retrievals analyzed later.



1060

Figure 4. (a) HSRL-2 observed 532 nm extinction profile along the ER-2 flight track on September 24, 2016. (b) GEOS baseline simulated 532 nm extinction profile along the same flight track. Dashed boxes near 9.5 UTC indicate the position of the profile compared to the P-3 profile in subsequent plots and referenced by the green star in Figure 1b.

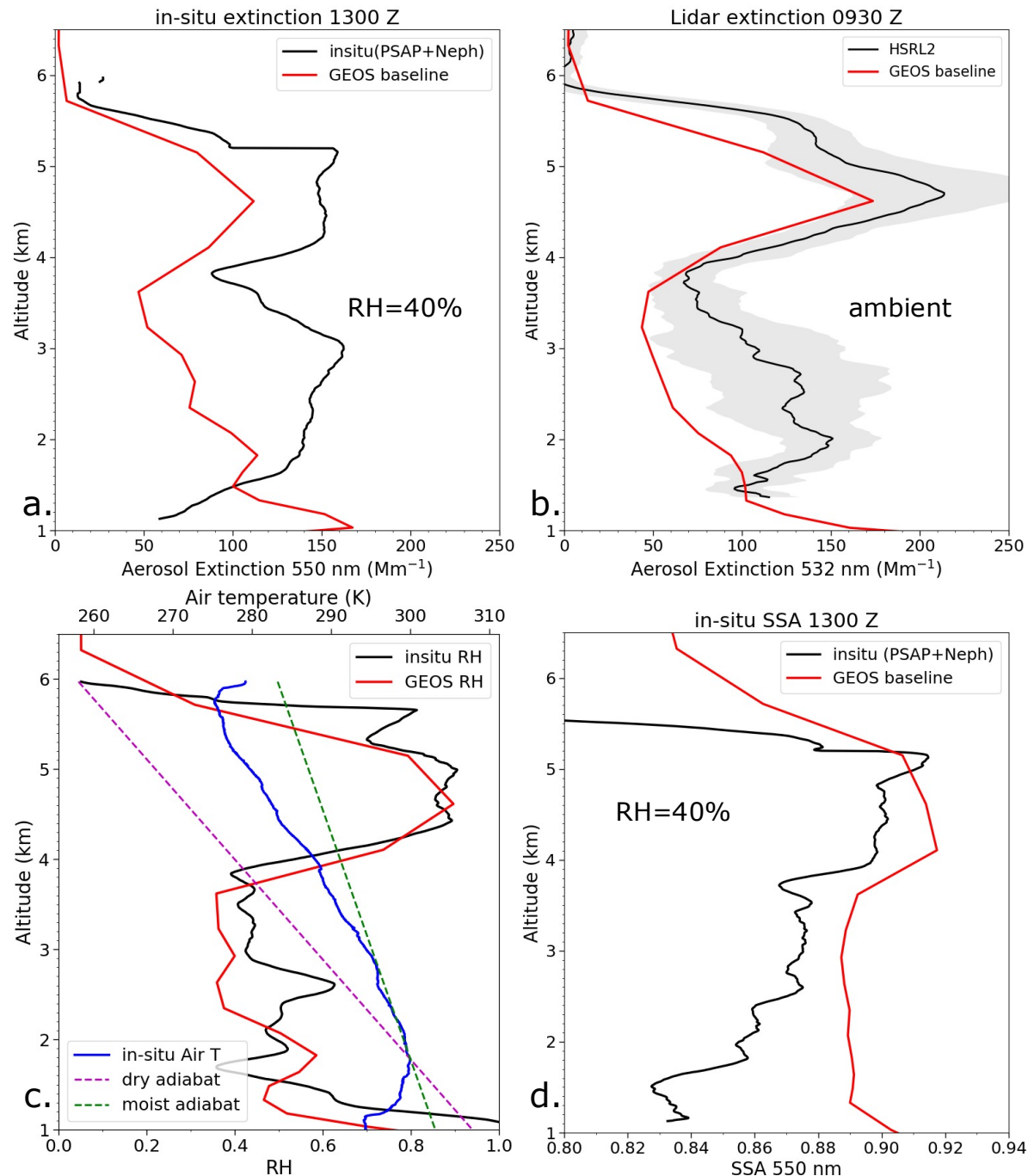


Figure 5. Profiles of the P-3 in situ measured 550 nm extinction (a) and ER-2 HSRL-2 lidar 532 nm extinction (b) for the point indicated by the green star in Figure 1b. Also shown are the P-3 measured relative humidity and ambient air temperature (c), along with the 550 nm single scatter albedo (d). On each plot the data are indicated by the black line and the GEOS baseline simulation on the profile are indicated by the red line.

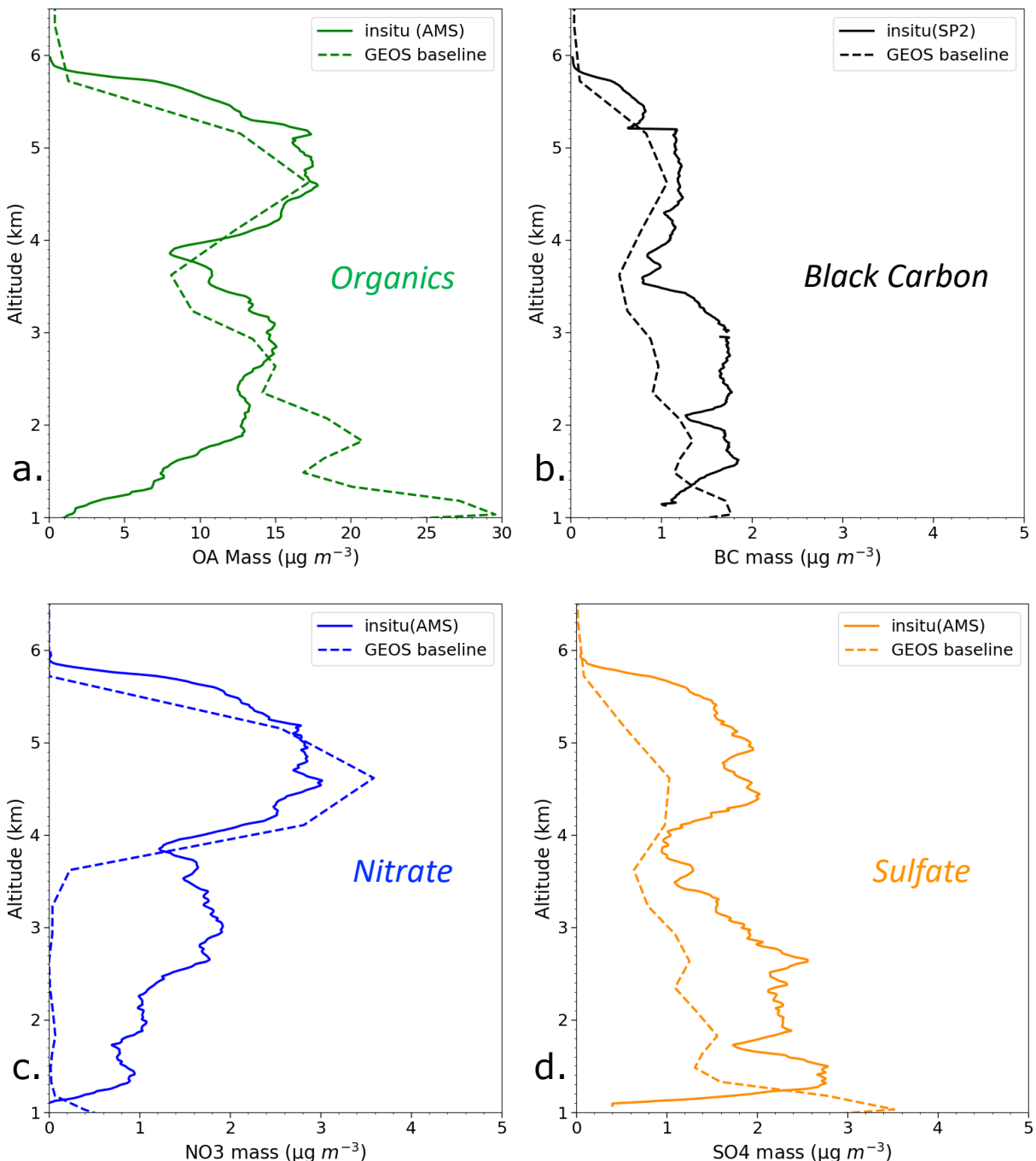
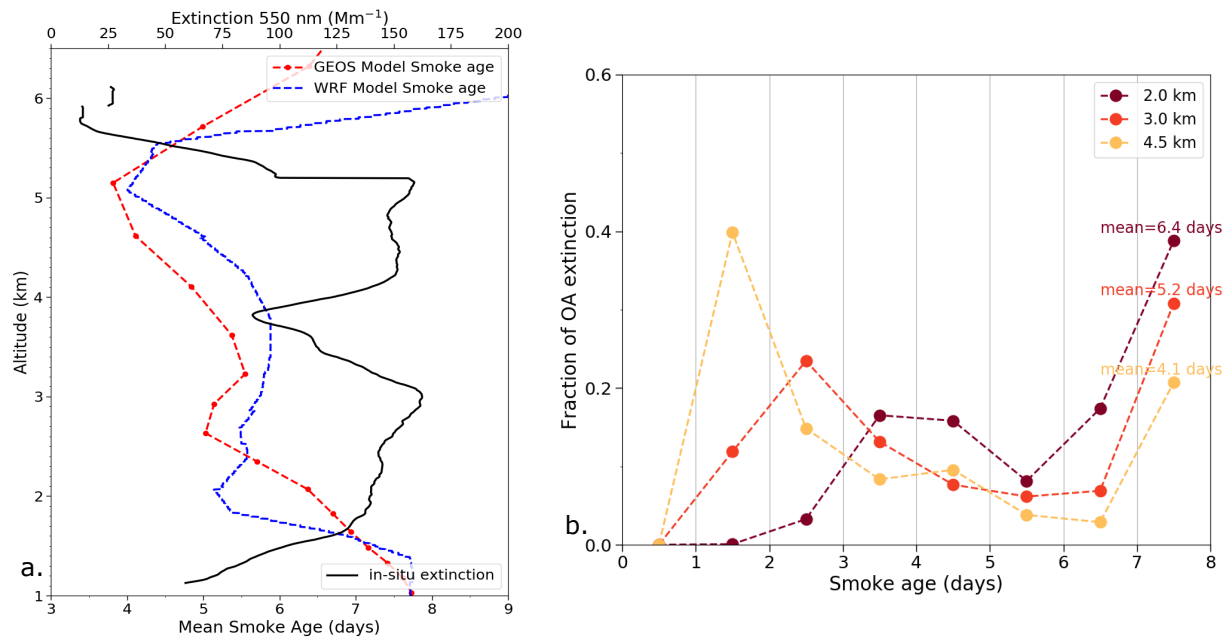
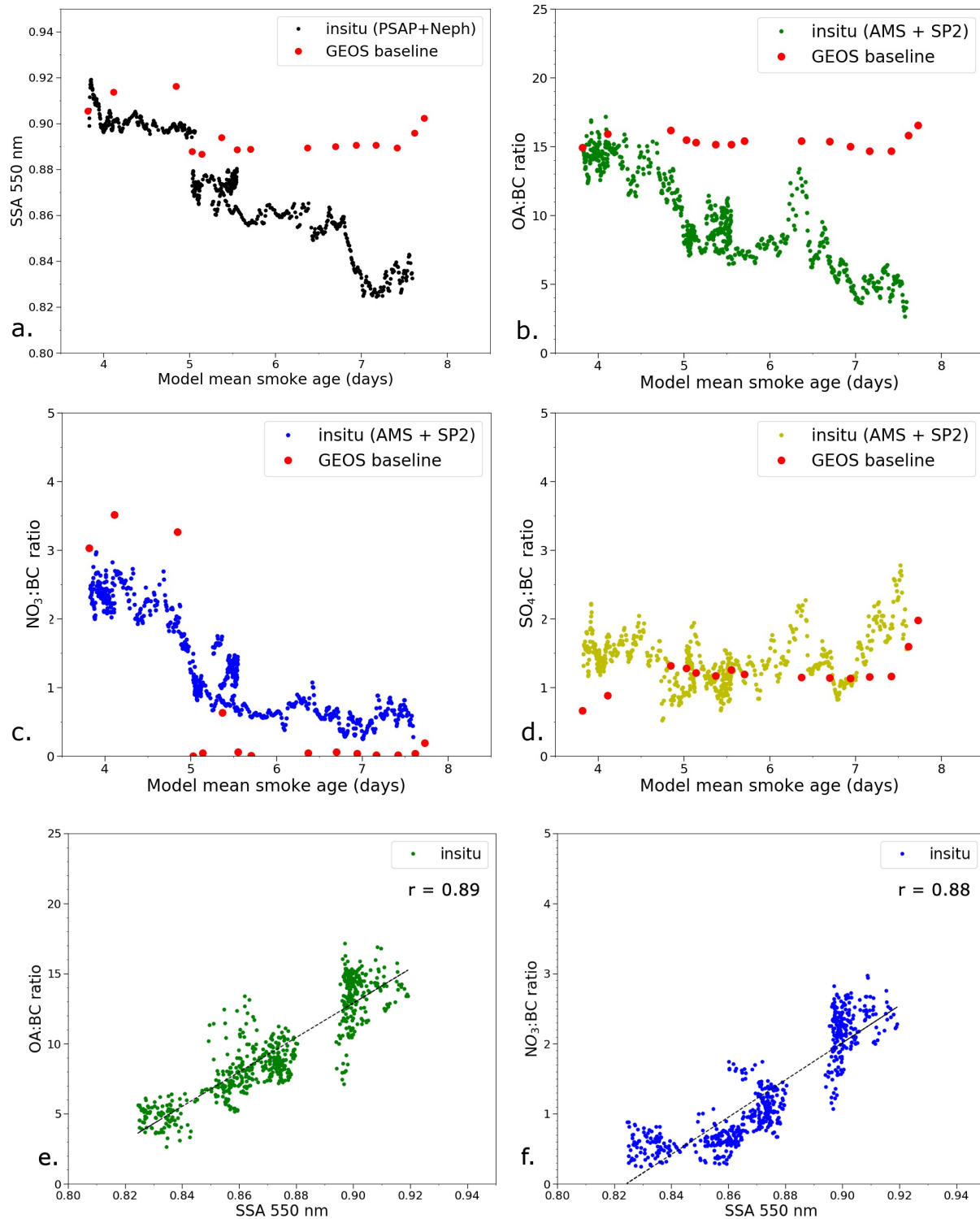


Figure 6. Comparison of the in-situ measured (solid lines) and GEOS baseline model-simulated (dashed lines) aerosol species mass concentrations on the P-3 profile flown near 12°S and 11°E on September 24, 2016. Shown are (a) organic aerosol, (b) black carbon, (c) nitrate, and (d) sulfate mass concentrations.



1080

Figure 7. (a) Comparison of the GEOS baseline simulated mean smoke age (red) to WRF-AAM simulated (blue) for the smoke profile near 12°S and 11°E flown by the P-3 on September 24, 2016. The in-situ extinction profile (black) is overlaid in (a) to demonstrate the differences in simulated smoke age between the multiple observed smoke layers. (b) Distribution of simulated smoke ages from the GEOS baseline simulation for the same plume profile at three different altitudes.



1085

Figure 8. Observed and simulated (a) SSA at 550 nm, (b) OA:BC ratio, (c) NO₃:BC ratio, and (d) SO₄:BC ratio for the smoke layers near 12°S and 11°E flown by the P-3 on September 24, 2016. All the results are sorted by mean smoke age from the GEOS baseline simulation. Also shown are the correlation of OA:BC ratio (e) and NO₃:BC (f) ratio against SSA.

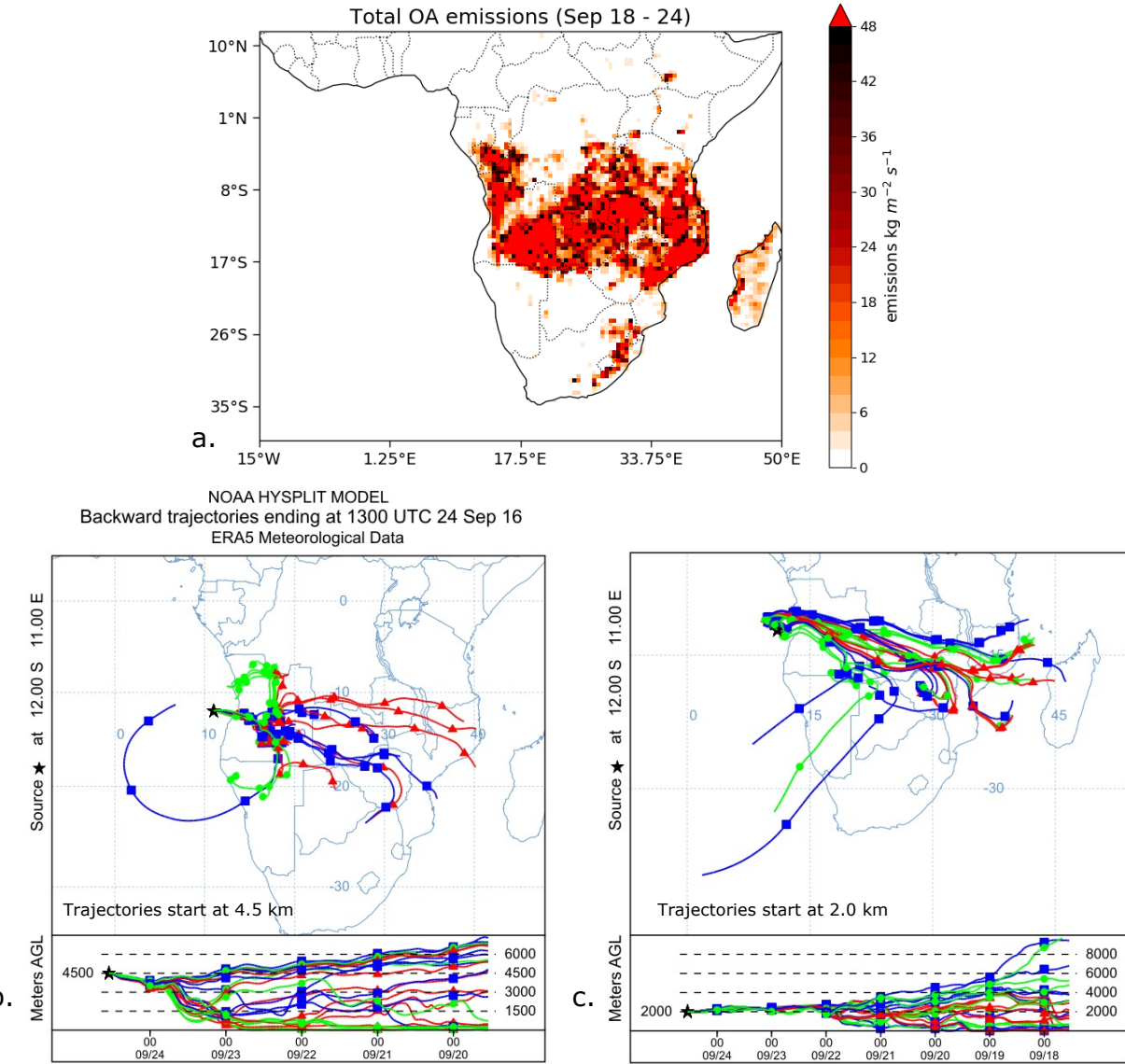


Figure 9. (a) Cumulative smoke emissions of OA over southern Africa in the week before the September 24, 2016, profile. Also shown are the ensemble of back trajectories calculated with the HYSPLIT model from the profile location initiated at 13 UTC on September 24, 2016, with trajectories ending at (b) 4.5 km and (c) 2 km altitude.

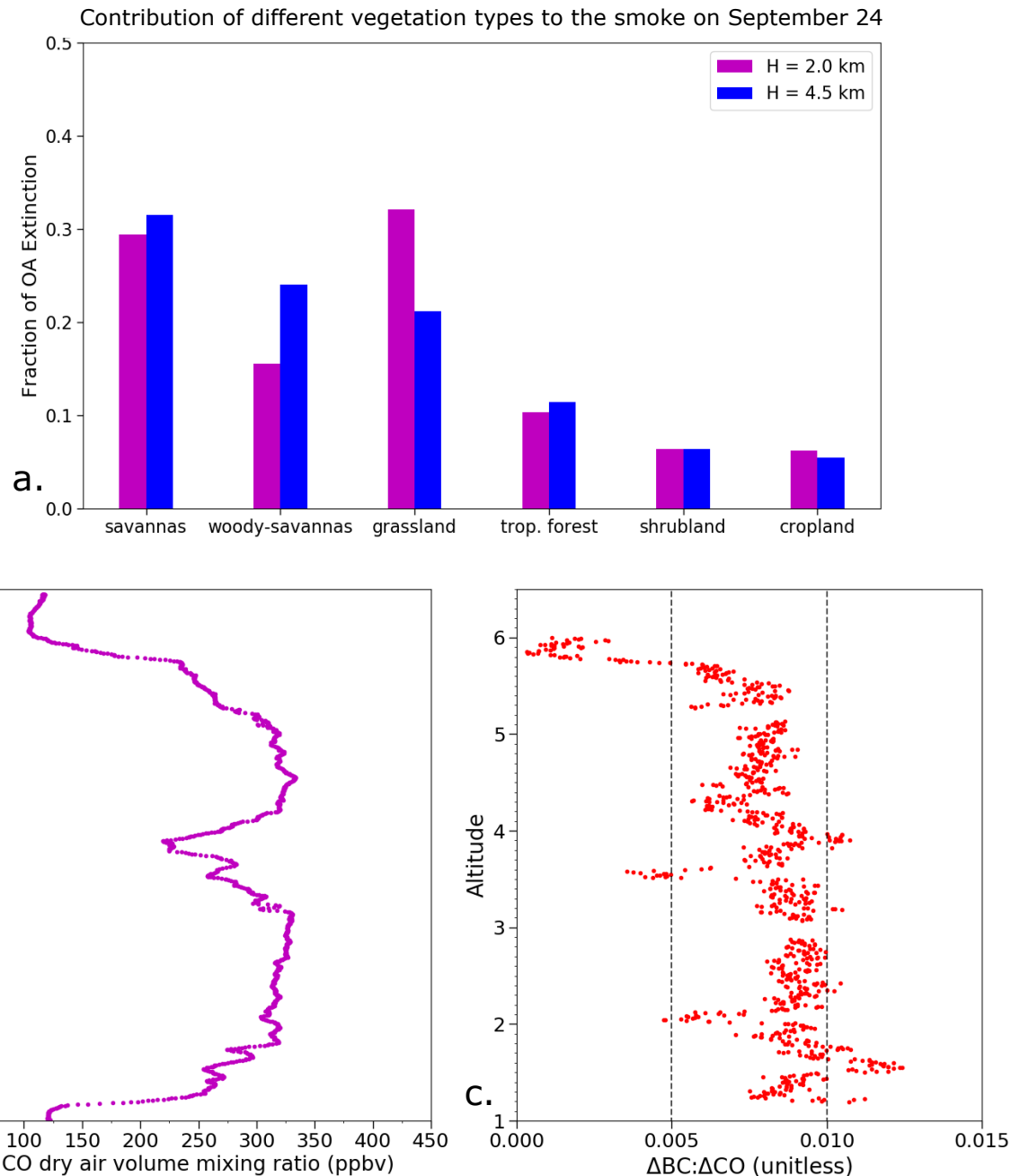
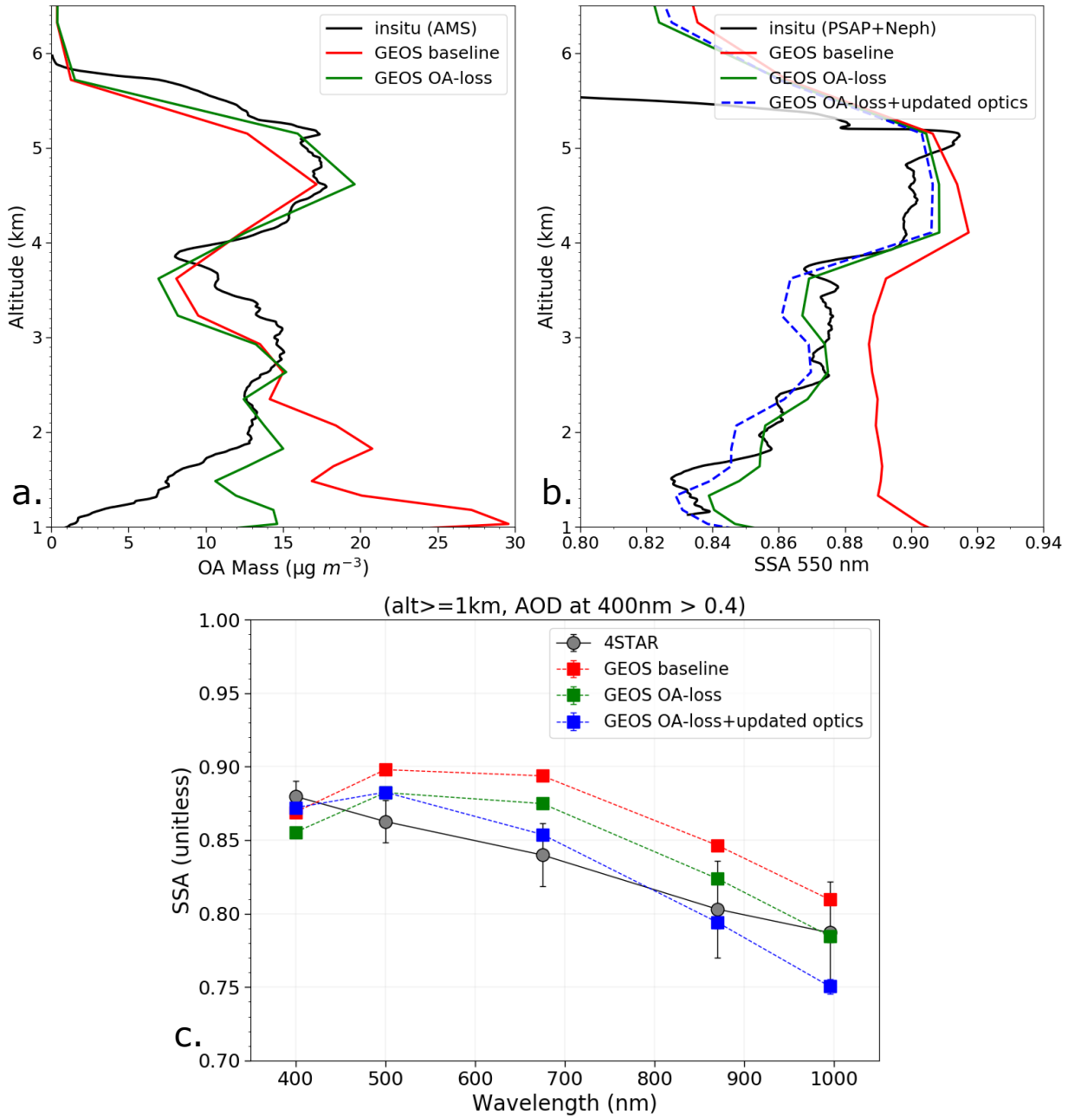


Figure 10. (a) Fraction of the OA extinction for the September 24, 2016, profile at 4.5 and 2 km altitude attributable to emissions from various types of vegetation burned. (b) P-3 observed carbon monoxide concentrations for the September 24, 2016, profile made near 12°S and 11°E. (c) Ratio of excess BC to carbon monoxide for the profile. Dashed lines demarcate regimes where smoldering (ratio < 0.005) and flaming (ratio > 0.01) conditions dominate.

1100



1105

Figure 11. Model agreement across different observational spaces for Sep 24 case: GEOS model-simulated (a) OA mass compared to AMS in-situ measurements, (b) dry SSA profile compared to in-situ (PSAP + Nephelometer) measurements, and (c) spectral column SSA compared to 4STAR retrievals averaged over three locations depicted by blue stars on Figure 3.

1110

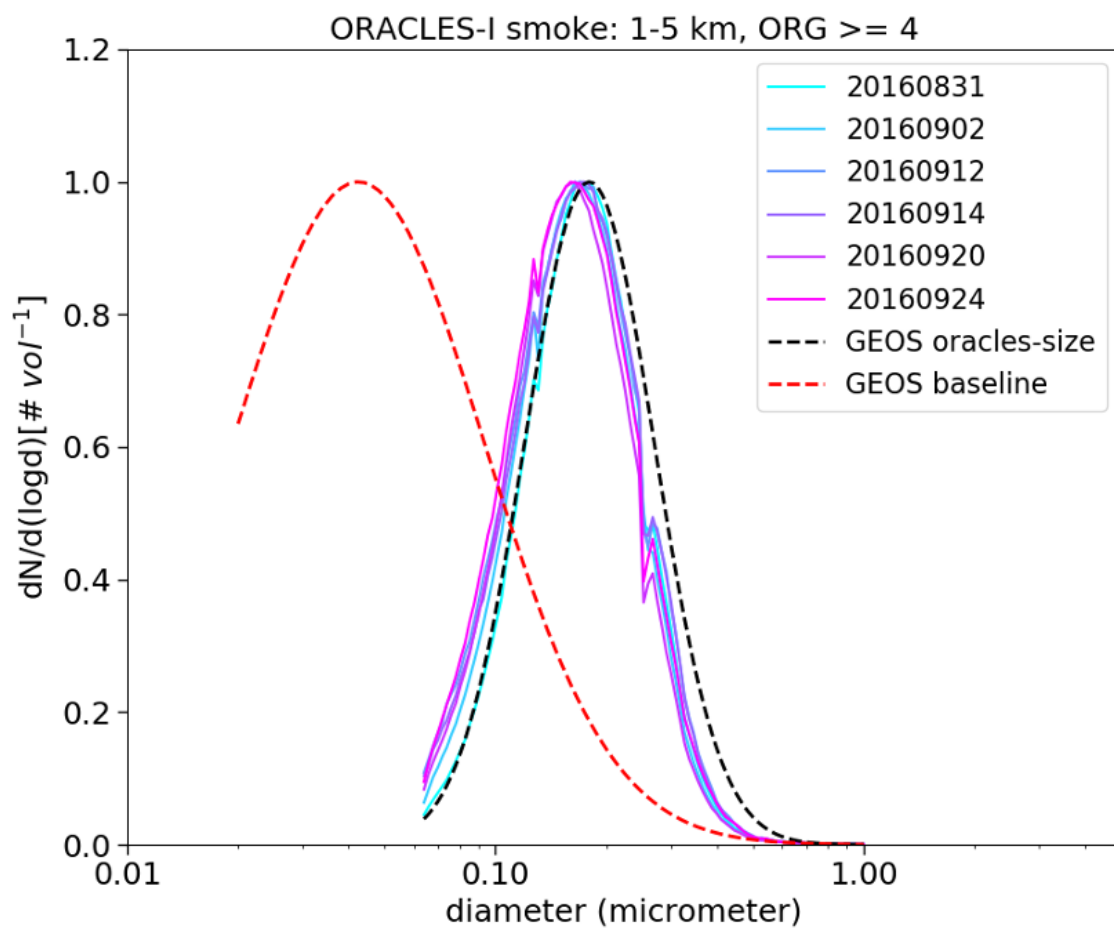
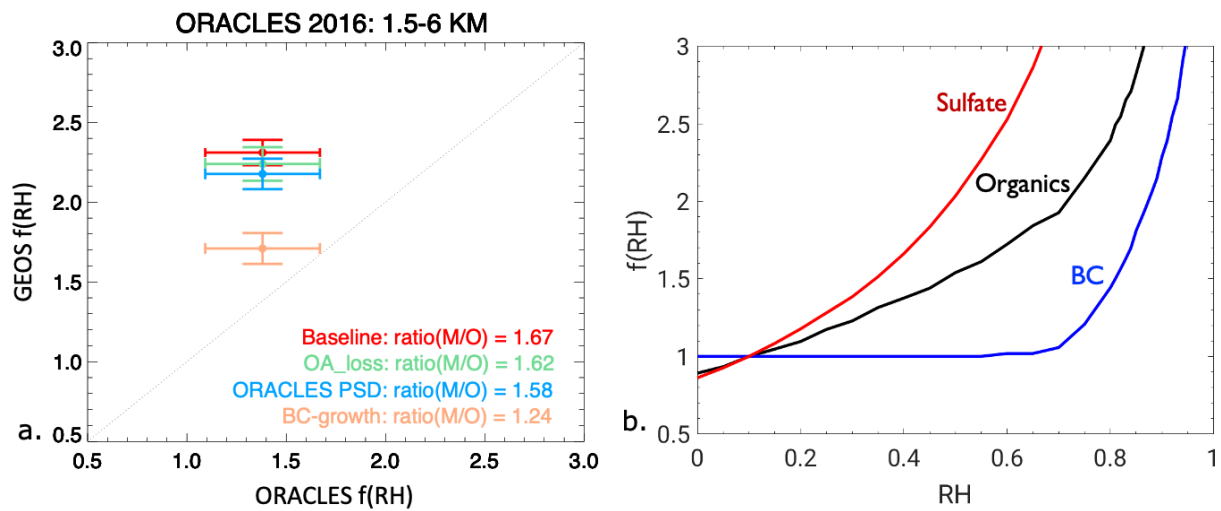


Figure 12. Comparison of GEOS baseline and adjusted particle size distribution for organic aerosol to ORACLES observations from the UHSAS instrument.



1120

Figure 13. (a) Comparison of simulated to observed $f(RH)$ in smoke plumes during the ORACLES-I deployment. Different cases of the model optical property assumptions are shown, and the ratio(M/O) reports the ratio of the model to the observed mean values. (b) Default $f(RH)$ in the GEOS lookup tables for sulfate, OA, and BC.

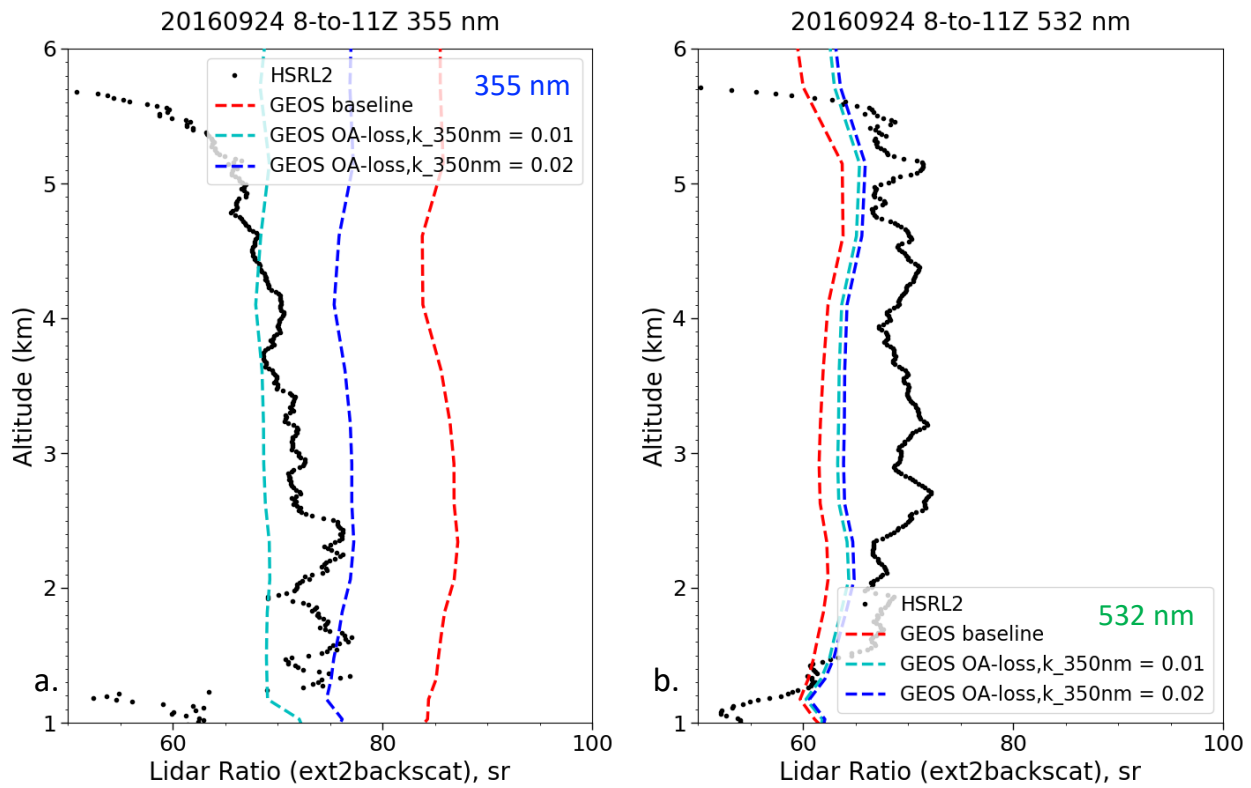


Figure 14. Comparison of the simulated and HSRL-2 observed lidar ratios at (a) 355 nm and (b) 532 nm for the profile near 12°S and 11°E on September 24, 2016.

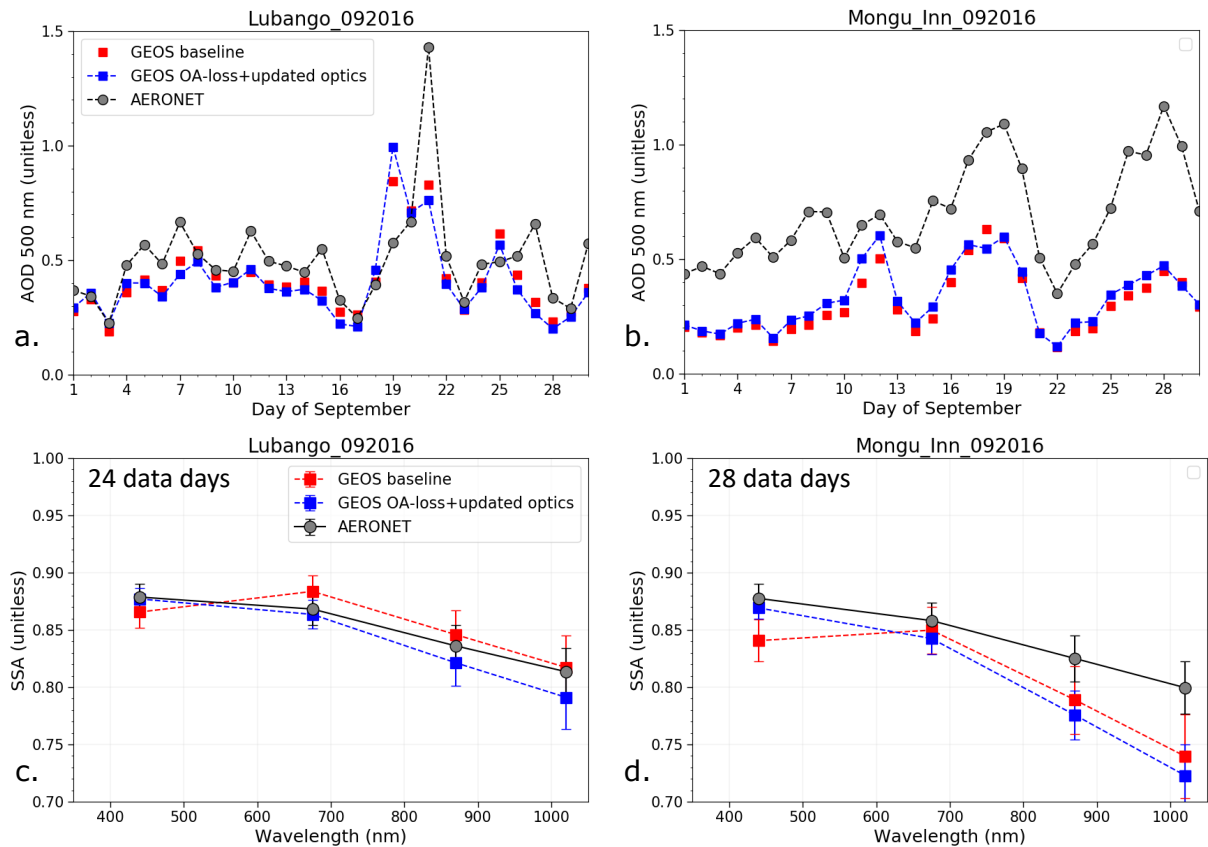


Figure 15. Comparisons of simulated and AERONET retrieved daily AOD at (a) Lubango and (b) Mongu_Inn sites over the continent for September 2016. The corresponding monthly mean spectral SSA are also compared between model simulations and AERONET (c) over Lubango and (d) Mongu_Inn, respectively.

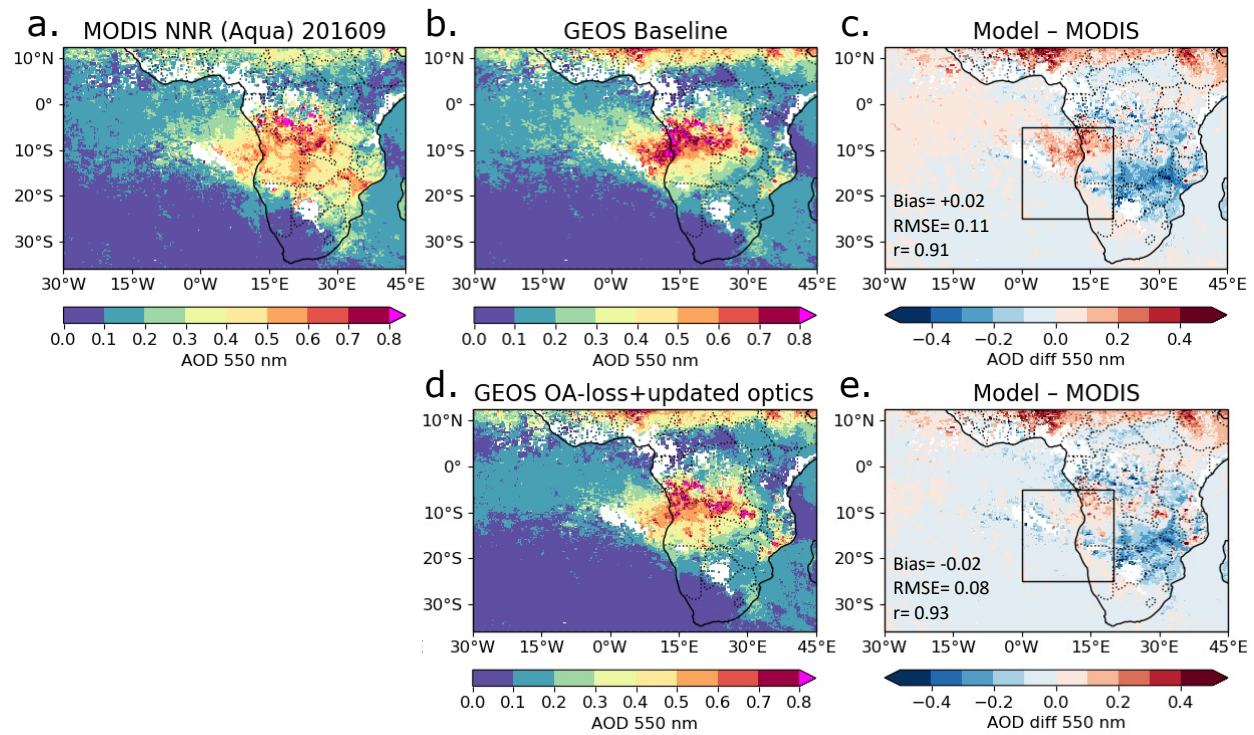


Figure 16. Comparisons of monthly mean AOD from (a) MODIS (Aqua) NNR retrievals, (b) GEOS baseline and (d) GEOS OA-loss+updated optics simulations. The corresponding AOD differences between the model simulations and MODIS observations are depicted in (c) and (e), respectively, along with the model performance metrics (mean bias, root-mean-square error or RMSE and Pearson correlation coefficient or r) for the region within the black box.

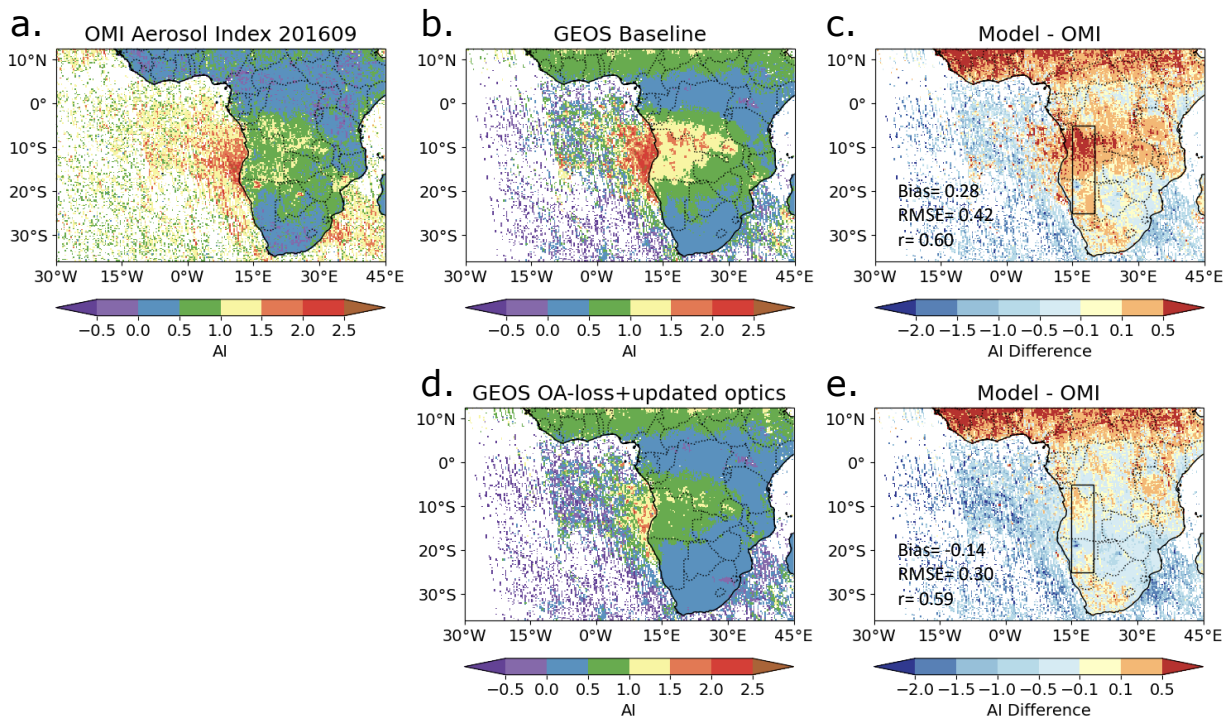


Figure 17. The September 2016 average OMI retrieved AI (a) and the simulated GEOS AI for the baseline (b) and OAloss+updated optics (d) model runs. The GEOS – OMI difference is shown compared to the GEOS baseline run (c) and the OAloss+updated optics runs (e), respectively, along with the model performance metrics (mean bias, root-mean-square error or RMSE and Pearson correlation coefficient or r) for the region within the black box.

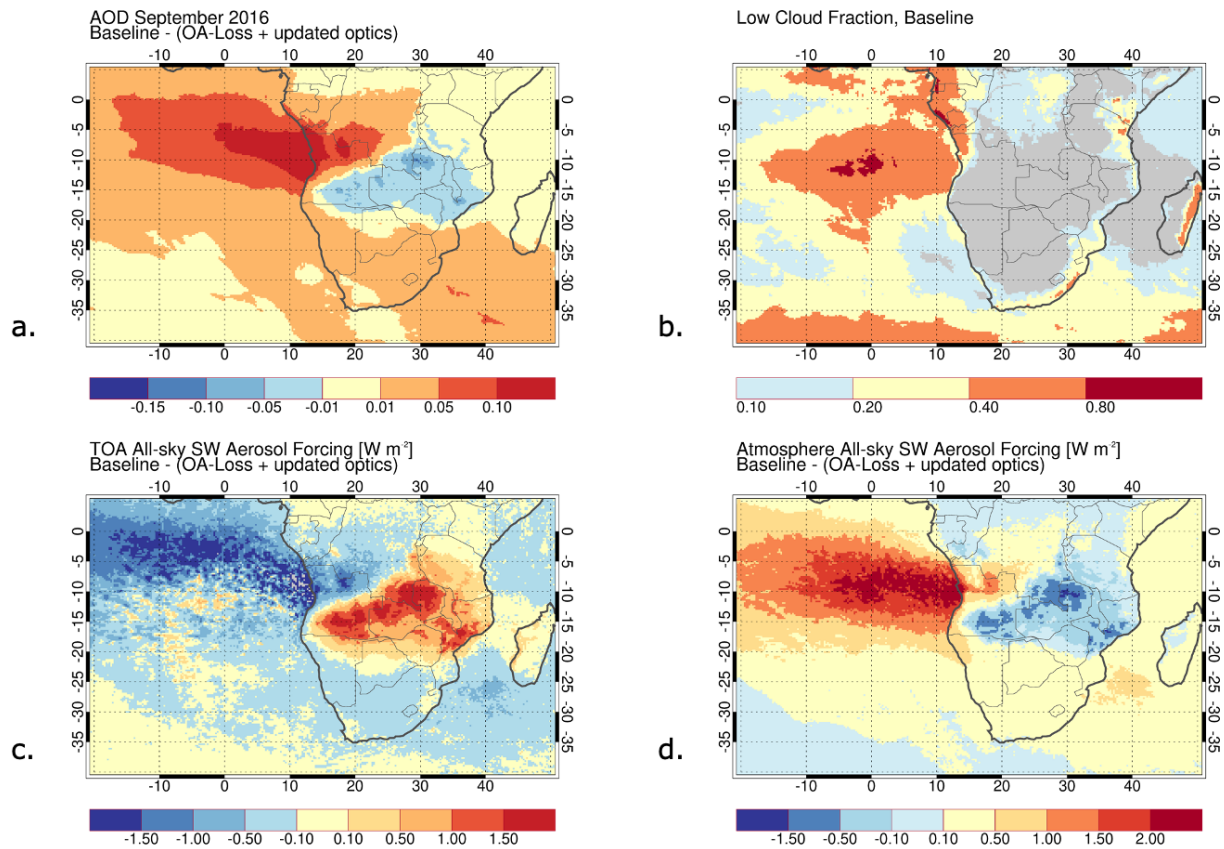


Figure 18. The September 2016 average GEOS-simulated (a) total 550 nm AOD difference between the baseline and OA-loss+updated optics model runs, (b) the low cloud fraction of the baseline run, (c) top-of-atmosphere all-sky shortwave aerosol forcing difference of the baseline and updated runs, and (d) the all-sky shortwave aerosol atmospheric heating difference of the baseline and updated runs. The grey area in (b) is cloud fraction less than 10%.

1145